Chemical Engineering Science 301 (2025) 120756

Contents lists available at ScienceDirect

Chemical Engineering Science

journal homepage: www.elsevier.com/locate/ces

Coalescence time of ellipsoidal-wobbling bubbles at surfactant-free interface: Experimental analysis and collision criteria

Eric M.G. Fontalvo [a], Paulo L.C. Lage [a,c,*], Juliana B.R. Loureiro [b,c]

[a] Programa de Engenharia Química, COPPE, Universidade Federal do Rio de Janeiro, Cidade Universitária, C.P. 68502, 21941-972, Rio de Janeiro, Brazil
[b] Programa de Engenharia Mecânica, COPPE, Universidade Federal do Rio de Janeiro, Cidade Universitária, C.P. 68503, 21945-970, Rio de Janeiro, Brazil
[c] Núcleo Interdisciplinar de Dinâmica dos Fluidos NIDF, Cidade Universitária, 21941-594, Rio de Janeiro, Brazil

ARTICLE INFO

Keywords:
Bubble coalescence
Bubble velocity
Bubble bouncing
Bubble shape
Gas-liquid interface

ABSTRACT

This work experimentally analyzed bubbles' coalescence with an air-water interface in the ellipsoidal-wobbling regime for different bubble approach velocities, encompassing the ranges of Eötvös, Weber, and Reynolds numbers of 2-3, 1-4, and 500-1100, respectively. We employed high-speed imaging to measure the bubbles' size, shape, velocity, coalescence time, and number of bounces at the interface. We investigated two criteria to determine the beginning of bubble-interface interaction ("collision"): the physical criterion, based on the distance between the bubble top surface and the interface, and the hydrodynamic criterion, based on the bubble velocity. Gamma distributions represented the coalescence times of bubbles at their terminal velocities well. We found a linear relationship between the coalescence time and the number of bounces. The hydrodynamic criterion was more consistent in representing our data on coalescence time.

1. Introduction

The coalescence of bubbles and droplets is important in many industrial and engineering applications, occurring in mass and heat transfer processes in bubble columns (Mitre et al., 2010; Zhang and Luo, 2020), mineral flotation (Neethling and Cilliers, 2001; Wang et al., 2020), gas and oil transportation (Mitre et al., 2014), wastewater treatment (Rubio et al., 2002), among others (Zawala and Malysa, 2011; Ribeiro and Mewes, 2007).

When two fluid particles, or a particle and an interface, approach each other ("collision"), a thin film of the continuous-phase fluid forms between them. For some conditions, this film drains to a critical thickness and breaks, joining the two interfaces leading to coalescence, in which the film drainage is considered the controlling factor (Marrucci, 1969; Jones and Wilson, 1978; Chesters and Hofman, 1982). From the bubble "collision", we can define two characteristic times: the iteration time, that is, the time that bubbles remain close to each other, and the coalescence time, defined as the time interval from the formation of the thin film to its rupture, which is approximately equal to the film drainage time (Chesters, 1991). Since not all "collisions" result in coalescence, the conditional probability of coalescence after a "collision" is the coalescence efficiency. The ratio between the coalescence and interaction times is used to model the coalescence efficiency (Liao and Lucas, 2010; Mitre et al., 2010). These characteristic times are functions of several parameters such as fluid properties, "collision" forces or velocities (Chesters, 1991; Ribeiro and Mewes, 2007), impurity or surfactant concentration (Craig et al., 1993; Liu et al., 2019, 2020), mobility and deformation of the interfaces (Vakarelski et al., 2018, 2020), gravity (Suñol and González-Cinca, 2019), among others (Ribeiro and Mewes, 2006).

The simplest system for the study of coalescence involves the collision of bubbles with flat interfaces (Kirkpatrick and Lockett, 1974; Doubliez, 1991; Sanada et al., 2005; Suñol and González-Cinca, 2010). The coalescence of bubbles with interfaces resembles an interplay between a small bubble and a bubble of infinite diameter for an infinite interaction time. This scenario always allows the drainage of the liquid film up to its critical thickness of rupture, leading to coalescence. Therefore, the probability of coalescence is always one, and any "collision" results in coalescence, as shown in Fig. 1a. This behavior contrasts with bubble-bubble interactions, where the coalescence efficiency can be null under some conditions, as depicted in Fig. 1b.

Many works analyzed the coalescence mechanisms. These works studied the liquid film thickness at the onset of drainage and just before rupture (Doubliez, 1991), the influence of the bubbles' approach veloc-

* Corresponding author at: Programa de Engenharia Química, COPPE, Universidade Federal do Rio de Janeiro, Cidade Universitária, C.P. 68502, 21941-972, Rio de Janeiro, Brazil.
E-mail addresses: efontalvo@peq.coppe.ufrj.br (E.M.G. Fontalvo), paulo@peq.coppe.ufrj.br (P.L.C. Lage), jbrloureiro@mecanica.coppe.ufrj.br (J.B.R. Loureiro).

https://doi.org/10.1016/j.ces.2024.120756
Received 29 May 2024; Received in revised form 10 September 2024; Accepted 16 September 2024
Available online 19 September 2024

Nomenclature

A	area
a	ellipse's semi-major axis
b	ellipse's semi-minor axis
$\mathbb{D}$	domain of N_b
d_e	equivalent diameter
F	cumulative gamma distribution
$\hat{F}$	empirical cumulative distribution
f_{acq}	frequency of acquisition
f_{pump}	frequency of pump
H_{ris}	rising height in mm
h_{ris}	rising height in pixels
h_f	bubble-interface distance
I	pixel intensity
I_b	mean intensity inside bubble
I_{max}	maximum intensity
I_{out}	mean intensity outside bubble
I_{thresh}	intensity threshold
i	first index/order
j	second index/order
L	calibration segment length
N	number of total elements in a sample
N_L	number of pixels in the calibration segment
N_b	number of pixels inside bubble
$N_{bubbles}$	number of injected bubbles
$N_{bounces}$	number of bounces
N_{out}	number of pixels outside bubble
N_{frames}	number of frames
N_{steps}	number of steps
N_x	number of pixels in x coordinate
N_y	number of pixels in y coordinate
$\hat{\mathbf{n}}$	unit normal vector
n	number of element in a sample
m_{ij}	ordinary moment of the bubble's binary image of order i and j in the x and y coordinates
$\mathbf{r}_s$	position vector
R_v	mean pump volumetric resolution
S	perimeter
s	standard deviation
T	temperature
$\overline{T}$	mean operational temperature of a data set
t	time
t_c	coalescence time
t_{coll}	collision time
t_{exp}	exposure time
t_f	final time
U	velocity
u	standard uncertainty
V	volume
V_{calc}	volume by pump calibration
V_{inj}	injected volume
X	x position in mm
x	pixel position in x coordinate
x_{bottom}	bubble bottom position in x coordinate
x_{top}	bubble top position in x coordinate
Y	y position in mm
Y_{int}	interface vertical position in mm
$Y_{int_{bottom}}$	bottom interface vertical position in mm
$Y_{int_{top}}$	top interface vertical position in mm
Y_{tip}	capillary tube tip vertical position in mm
y	pixel position in y coordinate
$y_{int_{bottom}}$	bottom interface vertical position in pixels
$y_{int_{top}}$	top interface vertical position in pixels
y_{top}	bubble top position in y coordinate

Greek letters

α	first parameter of the gamma distribution
β	second parameter of the gamma distribution
χ	generic measure
Δ	difference between magnitudes
η	generic power
Γ	gamma distribution
γ	incomplete gamma function
κ	scale factor
λ	eigenvalue
μ_{ij}	central moment of the bubble's binary image of order i and j in the x and y coordinates
ν_C	continuous phase dynamic viscosity
ν_D	dispersed phase dynamic viscosity
ρ_C	continuous phase density
ρ_D	dispersed phase density
σ	surface tension
θ	orientation of a with the horizontal
φ	generic variable
ζ	adjustment coefficients

Abbreviations

Eo	Eötvös number
Mo	Morton number
Re	Reynolds number
We	Weber number
ODR	orthogonal regression distance

ity, and the thickness of the film formed (Kirkpatrick and Lockett, 1974; Doubliez, 1991; Orvalho et al., 2015), the liquid film drainage rate using models based on lubrication theory (Reynolds, 1886; Chesters and Hofman, 1982; Zawala and Malysa, 2011; Manica et al., 2016), the number of bounces (Sato et al., 2011; Manica et al., 2016; Yang et al., 2019), and the influence of concentration of surfactants or additives that affect the interface's mobility (Craig et al., 1993; Malysa et al., 2005; Liu et al., 2019, 2020; Orvalho et al., 2021).

Some works specifically studied the coalescence between a rising bubble in still liquid and a flat gas-liquid interface without surfactants. Kirkpatrick and Lockett (1974) conducted experiments on bubble coalescence with flat interfaces to understand how approach velocity affects coalescence, finding that high approach velocities led to bubble bouncing at the interface. In contrast, low velocities resulted in rapid coalescence. Doubliez (1991) performed experiments using interference fringe shifts to measure the thickness of the thin liquid film between bubbles and interfaces, showing that it could reach the order of microns, concluding that the models based on the lubrication theory fail to predict the initial drainage stage. Doubliez (1991) discovers a single relationship between coalescence time and Weber number in low-viscosity liquids, where the number of bounces was the most influential parameter. Sanada et al. (2005) determined a critical Weber number for coalescence in low-viscosity liquids that agreed well with the experimental and theoretical results of Duineveld (1994), whose values are $We_{crit} = 0.104$ and 0.117, respectively. Suñol and González-Cinca (2010) observed air bubbles at an ethanol-air interface, concluding that the bouncing time increases linearly with the Weber number, and the height of the first bounce also depends linearly on the bubble equivalent diameter. Zawala and Malysa (2011) studied the influence of impact velocity and film thickness on coalescence time, finding that the higher the impact

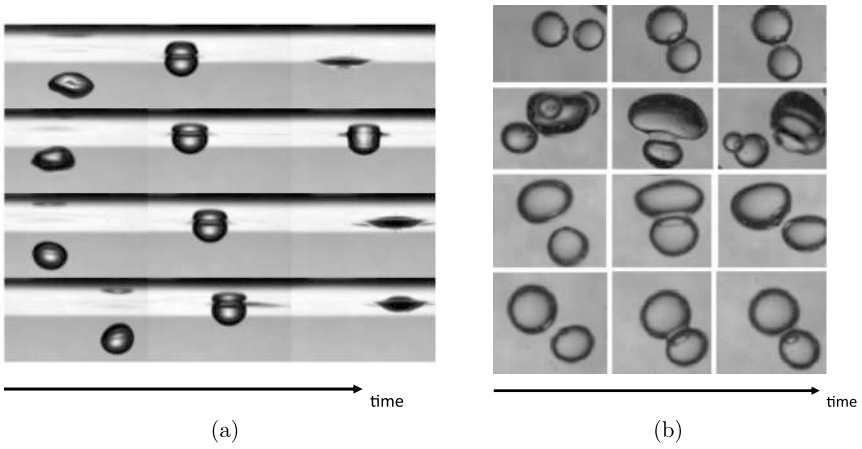

Fig. 1. Images of (a) bubbles bouncing and coalescing at the interface and (b) bubbles' collisions (Guinancio, 2015). No coalescence was observed in the latter experiments.

Table 1
Summary of literature review on bubble-interface coalescence experiments.

Author	Test section	Fluids	Conditions	d_e [mm]	Bubble Regime
Kirkpatrick and Lockett (1974)	A 3 in. diameter glass bell immersed in a water vessel Y_{int} = 4.5 to 35 mm	Air Water	T = 21±1 °C Mo = O(10^{-11}) $We^{(*)}$ = 0.76 - 3.0 $Re^{(*)}$ = 500 - 985	5	Ellipsoidal and Wobbling
Sanada et al. (2005)	Acrylic pool (15×15×40 cm) Y_{int} = 50 mm	Nitrogen Air/Silicone Oil	T = 20±3 °C Mo = O(10^{-10}) to (10^{-4}) We = 0.02 - 3.4 Re = 1 – 100	0.3 - 1.66	Spherical and Ellipsoidal
Suñol and González-Cinca (2010)	Methacrylate tank (25×25×25 cm) Y_{int} = 200 mm	Air Ethanol	T = 20±3 °C Mo = O(10^{-9}) We = 0.01 - 3 Re = 5 – 300	0.1 - 2.0	Ellipsoidal
Zawala and Malysa (2011)	Square glass column Y_{int} = 1.8, 2.2, 4.0 and 300 mm	Air Water	T = 22±1 °C Mo = O(10^{-11}) We$^{(*)}$ = 1.0 - 3.34 Re$^{(*)}$ = 263 - 600	1.0 - 1.6	Ellipsoidal
Sato et al. (2011)	Acrylic tank (12×12×60) cm	Nitrogen Air/Water	T = 25.8 °C Mo = O(10^{-11}) We$^{(*)}$ = 0.08 - 1.44 Re$^{(*)}$ = 97 - 648	0.62 - 1.56	Ellipsoidal
Present work	Polymethyl methacrylate cell Inlet: 4×5 cm Outlet: 12×5 cm Y_{int} = 10 and 25 mm	Air Water	T = 23–25 °C Mo = O(10^{-11}) We = 1 - 4 Re = 500 - 1100 Eo = 2 - 3	4	Ellipsoidal and Wobbling

(*) They were estimated in the present work based on data from the original reference.

velocity, the larger the bubble shape deformation and the liquid film thickness, resulting in more intense bubble bouncing, consistent with earlier findings. Sato et al. (2011) conducted experiments of bubbles bouncing at a free surface in pure water to verify the validity of a simple mass-spring model. The model agrees well with the experiments, and the time of the bubbles contacting the free surface was a function of the characteristic period of the oscillator.

Several works addressed the behavior of isolated bubbles ascending in a pool of a still liquid, predicting the regime from the Reynolds, Morton, and Eötvös dimensionless numbers (Clift et al., 2005; Tripathi et al., 2015). These dimensionless numbers, including the Weber number, are also used in analyzing coalescence (Sanada et al., 2009; Suñol and González-Cinca, 2010). For instance, Horn et al. (2011) presented a coalescence map for bubbles in surfactant-free aqueous electrolyte solutions, whose coordinates are the salt concentration and the bubble approach velocity, based on the results compiled by Kirkpatrick and Lockett (1974) and Lehr et al. (2002), among others. The critical Weber number determined agrees with the result of $We_{crit} = 1$ presented by Chesters and Hofman (1982) for two deformed bubbles approaching along their centerline. Their coalescence regime map defined the two regions separated by the critical Weber number as the rapid drainage and the elastic bounce regimes.

Although the literature on bubble coalescence at a gas-liquid interface is extensive, only some works have conducted experiments on bubble-interface coalescence in the ellipsoidal-wobbling regime. Therefore, more data on this process is necessary to model the phenomenon, given the diversity of theoretical assumptions and the lack of a precise definition of the initial drainage stage. Table 1 shows the experimental conditions carried out by Kirkpatrick and Lockett (1974), Sanada et al. (2009), Suñol and González-Cinca (2019), and Zawala and Malysa (2011).

Table 1 shows a need for experiments for bubbles of intermediate size (2.5-4.5 mm) in the literature. Therefore, in this work, we conducted experiments of 4 mm bubbles' coalescence with a flat, surfactant-free air-water interface.

We used advanced high-speed imaging techniques to measure bubble size, shape, velocity, and coalescence time (Versluis, 2013). We developed and reported new methods for determining the local bubble velocity and the uncertainties of the bubble image moments, which were used to obtain bubble size and position uncertainties. The Eötvös, Weber, and Reynolds numbers' ranges in our study are also shown in Table 1.

To calculate the coalescence time, we defined two "collision" criteria to determine the instant at which the bubble and interface begin their close contact, forming the thin liquid film: the physical criterion, based on the distance between the bubble's top and the static interface, and the hydrodynamic criterion, based on the bubbles' instantaneous velocity.

This work structure follows. Section 2 details the materials and methods employed, providing a clear understanding of how we measured the fluid properties, set up flow visualization, and conducted the experiments. Section 3 presents the data analysis, covering image acquisition, processing, bubble data measurements, the definition of relevant dimensionless numbers, and estimating the uncertainty of image moments. Section 4 presents the configuration of the experimental data sets. Section 5 presents and discusses the results, while Section 6 provides our conclusions.

2. Materials and methods

2.1. Materials

The properties of fluids were measured over the temperature range of 20 to 30 °C. The experiments utilized pure water as the continuous phase, produced by a Marte Pilsen-type distiller, filtered and demineralized. Its density was measured using an Anton Paar densimeter model DMA 4200M, with an accuracy of 10^{-4} g/cm^3. The viscosity was measured with a HAAKE MARS 40 rheometer, with a torque range of 20 - 200 nNm and a resolution of 0.1 nNm. Surface tension was measured by a KRUSS tensiometer, model K100C, using a Wilhelmy flat plate, with a deviation of 0.02 mN/m within a measured range of 1 to 2000 mN/m. Electrical conductivity was measured with a Metler Toledo conductivity meter model Seven Excellent, with a 0.001 μS/cm resolution. Ultra-pure water has a conductivity of 0.055 μS/cm at 25 °C. The density of the air, used as the dispersed phase, is calculated at sea level using a psychrometric chart.

Measured properties such as density, viscosity, and surface tension of the phases were correlated with models of one or two parameters capable of predicting fluid properties within the temperature range of 20 to 30 °C. The temperature of the liquid phase was measured with a digital thermometer with a resolution of 0.1 °C and expanded uncertainty of 0.13 °C for a coverage factor of 2. We used a Siberius digital hygrometer model HTC-2 with a resolution of 0.1 °C to measure room temperature and relative humidity, with measurement uncertainties of 0.30 °C and 1% RU, respectively, for a coverage factor of 2.

The Supplementary Material provides data and models used to calculate the fluid properties. The standard uncertainties were calculated using Type A and Type B evaluation methods (Joint Committee for Guides in Metrology, 2008). The water electrical conductivity was measured as 0.2 μS/cm at 23 °C.

The water and room temperatures were obtained from an average of four measurements taken during the experimental runs. Their combined standard uncertainty includes repeatability error, thermometer resolution, and data from a calibration certificate. The mean operating temperature, $\overline{T}$, was defined as the arithmetic average between the mean water and room temperatures. For two data sets presented in Section 4, $\overline{T} = 23.0 \pm 0.1$ °C.

Table 2
Phase properties at $\overline{T} = 23.0 \pm 0.1$ °C.

ρ_C [kg/m^3]	ν_C [mPa s]	σ [mN/m]	ρ_D [kg/m^3]
997 ± 7	0.964 ± 0.002	65.2 ± 0.1	1.184 ± 0.001

Table 2 presents the properties such as density, viscosity, and surface tension between the phases with their uncertainties at a 95% confidence level, calculated at the mean operating temperature of $\overline{T} = 23.0 \pm 0.1$ °C. The percent relative errors for the density and viscosity of the continuous phase (water), the surface tension, and the density of the dispersed phase (air) are 0.7%, 0.2%, 0.1%, and 0.08%, respectively.

2.2. Experimental setup

We used high-speed imaging to calculate the bubble characteristics such as volume, equivalent diameter, and instantaneous velocity in the stagnant liquid. The bubbles were filmed in the frontal plane of the test section of the experimental setup built by Coelho (2014) to observe coalescence. Fig. 2 presents a schematic illustration of the experimental setup. The unit was built to acquire experimental data on the coalescence efficiency of upward moving bubbles in a downward divergent flow channel. The experimental setup was adapted to experiments on bubble coalescence with a flat interface in a liquid pool. A capillary tube with a 2 mm inner diameter was vertically positioned at the bottom of the test section. This tube was connected to a 1000 µl syringe pump to guarantee slow air injection and achieve a single bubble formation at its tip. The syringe pump was fabricated using a Stratasys Objet1000 Plus 3D printer. Its injected volume per step was calibrated by adjusting the mean flowrate calculated based on the difference in mass and the actuation speed for the syringe pump, driven by an Arduino code. The equipment used in the calibration included a digital thermometer with a resolution of 0.1 ˚C, two 50 ml beakers, one 100 ml beaker (both cleaned and dried), and a BEL Engineering precision balance with a resolution of 1 mg.

The equipment used for the image acquisition consisted of a Phantom SpeedSense Lab M310 camera, a stroboscopic LED light, and a synchronizer/timer box. Illumination was homogenized using a diffuser sheet. The camera has a maximum acquisition rate of 3260 frames per second (fps) with an image resolution of 1280 × 800 pixels. Its sensor size is 25.6 mm × 16.0 mm of complementary metal-oxide-semiconductor (CMOS) type, allowing for monochrome or color imaging with 12-bit depth. Its pixel size is 20 × 20 µm. The camera was equipped with an AF Micro-Nikkor lens with a focal length of 60 mm and an aperture range of 2.8 to 32. The timer box was driven by a National Instruments counter/time board model PCIe-6612, which synchronizes the camera and LED to a computer featuring an Intel Xeon processor 2.5 GHz (8 CPUs) and 16 GB of RAM. Software Dynamic Studio 2015a of DANTEC Dynamics was employed to configure acquisition image parameters such as interframe, exposure, and illumination times.

2.3. Experimental procedure

Before each experimental campaign, the coalescence cell was removed from the apparatus, cleaned, and then rinsed three times with the same water used in the experiments. Next, we filled the test section with water, and slightly opened the VW4 valve in Fig. 2 to allow water to be slowly discharged into the tank to position the interface. We positioned the interface at the desired height above the tip of the capillary tube. During the experiments, the valve VW4 remained closed. Reference strips were placed on the sidewalls of the coalescence cell to facilitate the interface positioning. We took care to handle water without contaminating it. A water sample from each experiment was stored and dated for properties measurements. The duration of each experimental set, as well as the room and water temperatures, were recorded. The mean operating temperature was determined.

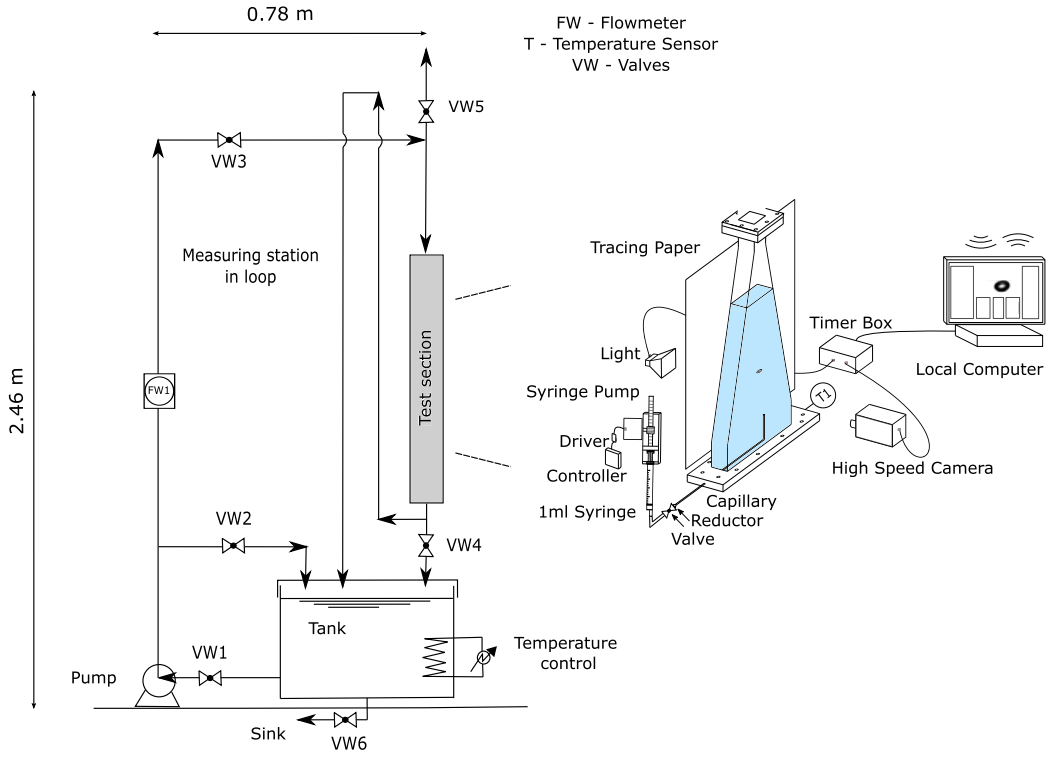

Fig. 2. Experimental Setup.

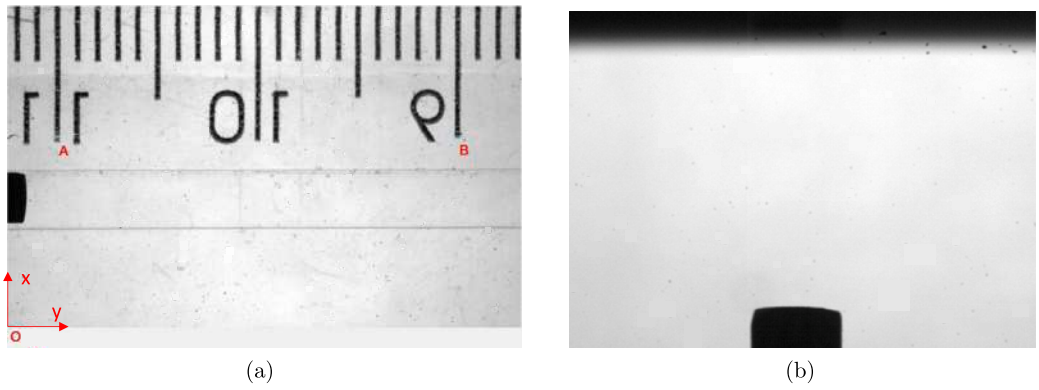

(a) (b)

Fig. 3. Image analysis: (a) estimation of the scale factor for calibration, and (b) image of the interface and capillary tube tip.

The camera's field of view was adjusted to capture the bubble detachment, ascension, collision, and coalescence with the interface. The focus and effective aperture of the diaphragm lens were adjusted manually. The distance between the object and the camera must exceed the lens' minimum focal distance. Acquisition parameters were synchronized with the timer box and modified using the Dynamic Studio software. We used an illumination time shorter than the exposure time to prevent pixel saturation, thus reducing the motion blur (Versluis, 2013). The software's graphical interface allowed for a preview visualization of the camera view with the adjusted parameters. If saturation occurred, we decreased the diaphragm aperture or the exposure time.

Each experimental set comprises several runs, each providing images with the chosen number of frames in single-frame mode at the selected acquisition frequency, given in frames per second (fps). In the syringe pump software driver, we configured the number of steps and the actuation frequency of the pump in steps per second (steps/s).

3. Data analysis

The image-based measurement procedure comprises three stages: image acquisition, digital processing, and measurement extraction. The first stage (acquisition) is sensitive to external parameters such as vibrations, light flicker, focus, and hardware characteristics like spatial resolution, shutter, and lens distortion. These factors influence the second stage (image processing), which propagates these effects to the measurements resulting from the third stage (De Santo et al., 2004). The following subsections describe the image acquisition, the image processing, and the measurements' extraction for the bubbles' characteristics.

3.1. Image acquisition

The first step in analyzing an image is calibration. For calibration, we cleaned a 30 cm transparent ruler and positioned it immersed in the water at the center of the cell aligned with the outlet of the capillary tube tip, as shown in Fig. 3a. The points O, A, and B in Fig. 3a were

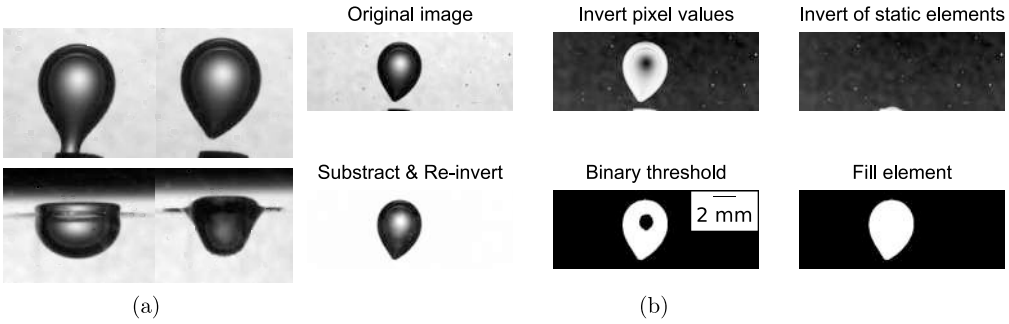

Fig. 4. Image processing: (a) bubble detachment and coalescence, and (b) sequence of steps done on the image processing.

Fig. 5. Pixel intensity values near to bubble interface and resulting binary image.

set respectively at the origin of the image coordinate plane xy and at two positions separated by a known absolute length, L, provided by the calibration target. Fig. 3b shows that the capillary tube and interface appear black, with a gradual transition from white to black for the latter due to interface refraction.

From the number of pixels in the image calibration segment, N_L, and the absolute distance in mm, L, we calculated the scale factor as follows:

$$\kappa = \frac{N_L}{L} \tag{1}$$

A new $x'y'$ coordinate system was defined for each bubble, whose origin is the initial position of its barycenter, given by the coordinates in pixels (x_{c_0}, y_{c_0}). The positions in the $x'y'$ plane are:

$$x' = x_c - x_{c_0} \quad ; \quad y' = y_c - y_{c_0} \tag{2}$$

Once the conversion factor from pixel to mm is known, the position of a pixel in mm in the $x'y'$ plane of the image, representing the horizontal and vertical axis, respectively, is given by:

$$X' = \frac{x'}{\kappa} \quad ; \quad Y' = \frac{y'}{\kappa} \tag{3}$$

3.2. Image processing

The intensity of a pixel, $I(x, y)$, in a grayscale image, is given by an integer value from 0 to $(2^{bits} - 1)$, where $bits$ is the number of bits uses to define each pixel, that is, the number of represented grayscale tones. The values of x and y are the pixel positions in the image coordinate plane, also represented by integer values, with $x = 1, ...N_x$ and $y = 1, ..., N_y$, for images with a resolution of $N_x \times N_y$ pixels. For instance, in 12 bits, the image can store up to 4096 levels of gray, where usually black corresponds to 0 and white to 4095. In the case of a binary image, there are only two values for each pixel, 0 and 1, corresponding to black and white, respectively.

3.2.1. Bubble image processing

Fig. 4a demonstrates the initial manual image filtering conducted for every acquired image set. This step is crucial as it delineates the phenomenon of interest from the detachment of the bubble from the capillary to its coalescence with the interface. The detachment corresponds to the neck break that connects the bubble to the capillary, while the coalescence corresponds to the rupture of the liquid film between the bubble and the interface. Following this, a series of sequential operations were systematically applied to each image to identify the bubbles and their characteristics. The sequence of image processing steps and the resulting image at each stage are clearly depicted in Fig. 4b.

We employed the following image operations: *pixel inversion*, *invert image subtraction* to eliminate static elements, *pixel inversion* to return to the values of $I(x, y)$ of the original image, *image binarization* using Eq. (4) with the threshold intensity, I_{thresh}, determined by Otsu's method (Otsu, 1979), *bubble filling* to eliminate the dark region in its center, and *image masking* to remove uninteresting areas or elements defined in a mask from the image set, particularly reflections of the bubble when it is close to the interface.

$$I(x, y) = \begin{cases} 0 & , \text{ if } I(x, y) > I_{thresh} \\ 1 & , \text{ otherwise} \end{cases} \tag{4}$$

Fig. 5 shows the intensity values close to the bubble interface for a 12-bit grayscale image on the left and the resulting image of the above processing that generates the filled binary image with $I = 1$ inside the bubble on the right.

The algorithm also executes the following steps to determine the uncertainties in the image moments due to the bubble image binarization.

- Using the final binarized image of the bubble, it calculates the number of pixels inside the bubble, N_b, and outside, N_{out}, as being the difference between the total number of pixels $(N_x \times N_y)$ and N_b.
- Using the original grayscale image of the isolated bubble, it determines the ΔI_{thresh} as 5% of the difference between the mean intensity values inside, I_b, and outside the bubble, I_{out}, such that

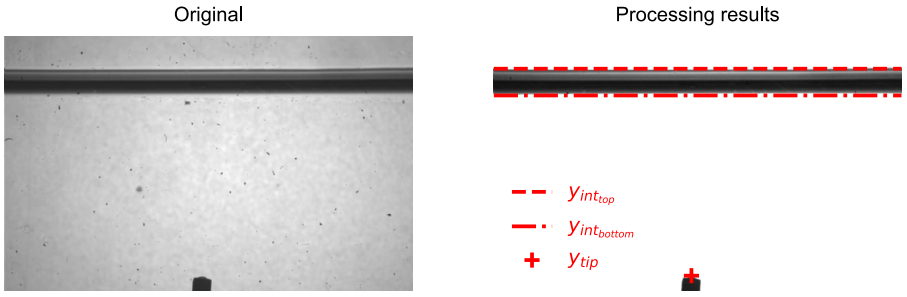

Fig. 6. Interface image processing.

$\Delta I_{thresh} = 0.05|I_{out} - I_b|$, where $I_{out} = 1/N_{out} \sum_{k=1}^{N_{out}} I_k$ and $I_b = 1/N_b \sum_{k=1}^{N_b} I_k$.

- It determines the perturbed thresholds of intensity $I_{thresh} + \Delta I_{thresh}$ and $I_{thresh} - \Delta I_{thresh}$ and the resulting values of N_b^+ and N_b^-, respectively

The algorithm calculates the zeroth and first image moments of the binary image from their definitions:

$$m_{ij} = \iint_{\mathbb{D}} x^i y^j I(x,y) dx dy = \sum_{k=1}^{N_b} x_k^i y_k^j \Delta x \Delta y, \quad (ij) = (00), (10), (01) \tag{5}$$

where $\Delta x = \Delta y = 1$ in pixel units. The zero-order moment, m_{00}, corresponds to the area of the bubble in pixel units, whose barycenter in the xy coordinates is:

$$x_c = \frac{m_{10}}{m_{00}} \quad ; \quad y_c = \frac{m_{01}}{m_{00}} \tag{6}$$

Then, it computes the second-order central moments of the binary distribution, $\mu_{ij}, i + j = 2$, from:

$$\mu_{ij} = \iint_{\mathbb{D}} (x - x_c)^i (y - y_c)^j I(x,y) dx dy = \sum_{k=1}^{N_b} (\Delta x_k)^i (\Delta y_k)^j \Delta x \Delta y \tag{7}$$

where $\Delta x_k = x_k - x_c$ and $\Delta y_k = y_k - y_c$.

Finally, the algorithm recalculates the image moments using the perturbed threshold intensities $I_{thresh} + \Delta I_{thresh}$ and $I_{thresh} - \Delta I_{thresh}$. Section 3.5 explains the calculation of the moments' uncertainties due to the binarization process.

Besides, for each bubble image, we also determined the coordinates of the lower $(x,y)_{bottom}$ and upper $(x,y)_{top}$ corners of the rectangle that contains the bubble projected area.

3.2.2. Gas-liquid interface image processing

The interface image processing follows a procedure similar to bubble image processing. The procedure begins with binarizing the original grayscale image using a threshold determined by Otsu's method, as given in Eq. (4). This results in a white interface on a black background. Image masking is then applied to remove all image features except the capillary tube and the interface.

To determine the interface vertical position, the coordinates in pixels of the lower $(y_{int_{bottom}})$ and upper $(y_{int_{top}})$ corners of the rectangle containing the interface projected area are determined. Thus, we defined the vertical interface position as:

$$y_{int} = \left(y_{int_{top}} + y_{int_{bottom}} \right) / 2 \tag{8}$$

Fig. 6 shows the resulting image of the interface processing, indicating the interface's top and bottom positions and the vertical position of the capillary tube tip in pixel units.

The rising height is the vertical distance between the interface position and the capillary tube tip calculated as:

$$h_{ris} = y_{int} - y_{tip} \tag{9}$$

We used Eqs. (1) and (3) to calculate the vertical positions of the interface, Y_{int}, and capillary tube tip, Y_{tip}, and the rising height, H_{ris}, in mm. We assumed the uncertainty of the interface position as half the difference between the top and bottom positions, determining the uncertainty in the rising height from error propagation.

3.3. Bubble data measurements

3.3.1. Bubble volume and shape

Assuming that the bubble is a spheroid, the second-order central moments calculated using Eq. (7) were used to calculate its major and minor semi-axes and the orientation of the major semi-axis with the horizontal (Hu, 1962). The major, a, and minor, b, semi-axes of an ellipse are given by:

$$a = \left[\frac{16\lambda_1^3}{\pi^2 \lambda_2} \right]^{1/8} \tag{10}$$

$$b = \left[\frac{16\lambda_2^3}{\pi^2 \lambda_1} \right]^{1/8} \tag{11}$$

where λ_1 and λ_2 are the eigenvalues of the covariance matrix of the second-order central moments, given by:

$$\lambda_{1,2} = \frac{\mu_{20} + \mu_{02}}{2} \pm \frac{\sqrt{4\mu_{11}^2 + (\mu_{20} - \mu_{02})^2}}{2}, \lambda_1 > \lambda_2 \tag{12}$$

The angle of the major semi-axis with the x-coordinate axis is calculated as follows:

$$\theta = \frac{1}{2} \tan^{-1} \left(\frac{2\mu_{11}}{\mu_{20} - \mu_{02}} \right) \tag{13}$$

We computed the inverse tangent function in the above equation using the function $atan2(2\mu_{11}, \mu_{20} - \mu_{02})$ as it gives θ in the correct quadrant.

The complete analysis of the image moments and their interpretation using the elliptical shape assumption is presented in the Supplementary Material.

The bubble's projected area approximated as an ellipse was calculated from its major and minor semiaxis as:

$$A_{ellipse} = \pi ab \tag{14}$$

The bubble's volume was approximated to that of an oblate or prolate spheroid, depending on the orientation of its semi-axes, as follows:

$$V = \frac{4\pi}{3} abc \tag{15}$$

where

$$c = \begin{cases} a, & \text{if } -45° < \theta < 45° \\ b, & \text{otherwise} \end{cases} \tag{16}$$

The bubble's equivalent diameter is defined by:

$$d_e = \sqrt[3]{6V/\pi} \tag{17}$$

To evaluate mean values for area, volume, and velocity of each bubble with minimal interference from its detachment and "collision" with the interface, we used just the images acquired when the bubble barycenter was in the middle half of the available liquid height, that is, $Y'_c \in [Y'_{min} + \Delta Y', Y'_{max} - \Delta Y']$, where $Y'_{min} = 0$, $Y'_{max} = \max\{Y'_{top}\}$, and $\Delta Y' = 0.25 Y'_{max}$.

Considering N images, the bubble's mean area and volume were calculated using the following weighted average:

$$\overline{\varphi} = \frac{\sum_{n=1}^{N} \varphi_n \omega_n}{\sum_{n=1}^{N} \omega_n} \tag{18}$$

where φ_n is the variable value, and ω_n is the corresponding weight given by the reciprocal of the experimental measurement uncertainty $\omega_n = 1/u(\varphi_n)$. The sample standard deviation was also calculated as $s_\varphi = \sqrt{\frac{\sum_{j=1}^{N}(\varphi_j - \overline{\varphi})^2}{N-1}}$. The mean equivalent diameter was determined from the bubble's mean volume using Eq. (17).

The mean velocity was estimated as the slope of the linear model:

$$Y' = \overline{U}_{Y'} t + Y'_0 \tag{19}$$

whose parameters were adjusted using the Orthogonal Distance Regression (ODR) method (Boggs et al., 1989).

To evaluate the accuracy and repeatability of the $\overline{d}_e$ and $\overline{U}_{Y'}$ data for each experimental data set, we determined the arithmetic means of their determination errors at the 95% confidence level and their standard deviations, both expressed as percentages of the corresponding mean values.

3.3.2. Bubble's instantaneous vertical velocity

The vertical component of the bubble's velocity at a given time instant, t, is obtained by adjusting the linear model $Y'_c(t) = \zeta'_0 t + \zeta'_1$ to a (t, Y'_c) data set in a time interval around t. The ζ'_0 and ζ'_1 coefficients were also estimated using the ODR method (Boggs et al., 1989), being $U_{Y'_j} = \zeta'_0$. The data set is symmetrically distributed around t in a moving window given by $\Delta t = 2n\Delta t_{min}$, where $\Delta t_{min} = 1/f_{acq}$. The window contains $2n+1$ points from $Y'(t_j - n\Delta t_{min})$ to $Y'(t_j + n\Delta t_{min})$, or Y'_{j-n} to Y'_{j+n}, considering $Y'_j = Y'(t_j)$.

For the initial ($j < n$) and the final ($j > N - n$) time instants, the fitting of the data sets in the interval from Y'_0 to Y'_n, and from Y'_{N-n} to Y'_N, respectively, determines the instantaneous velocity. The first and the last velocity values were calculated by forward and backward finite differences, respectively.

We assumed that there is an agreement between the instantaneous velocity calculated using two different windows (Δt_1 and Δt_2) when there is a large percentage (>95%) of their points satisfies the following condition:

$$\frac{|U_{Y'}(t, \Delta t_2) - U_{Y'}(t, \Delta t_1)|}{[u[U_{Y'}(t, \Delta t_2)]^2 + u[U_{Y'}(t, \Delta t_1)]^2]^{0.5}} < 1 \tag{20}$$

3.3.3. Estimation of coalescence time

The drainage of a thin liquid film formed when the bubble and the gas-liquid interface are very close to each other controls the coalescence time. Since the thin film thickness is of tenths of micrometers (Doubliez, 1991), image analysis cannot resolve it. Thus, we defined the coalescence time as the time interval between the instant when the bubble finally coalesces with the interface, t_f, and the time, t_{coll}, which is the onset of formation of the thin liquid film between the interfaces. Thus, the coalescence time is defined by:

$$t_c = t_f - t_{coll} \tag{21}$$

Since the image analysis cannot resolve the liquid film thickness, to determine t_{coll}, we defined two criteria for its onset: the first time the bubble gets close to the gas-liquid interface, that is, at the first "collision." The physical collision criterion (PCC) defines t_{coll} when, for the first time, the distance between the bubble's top surface and the interface is null, considering its uncertainty:

$$t_{coll} = t_j \quad \text{if } h_{f_j} - u(h_{f_j}) \le 0 \tag{22}$$

where h_f at the time instant t_j is the distance between positions of the top surface of the approaching bubble, Y_{top}, and the static interface, Y_{int}, given by:

$$h_{f_j} = Y_{int} - Y_{top_j} \tag{23}$$

The hydrodynamic collision criterion (HCC) defines t_{coll} when, for the first time, the bubble's vertical velocity is null considering its uncertainty:

$$t_{coll} = t_j \quad \text{if } U_{Y'_j} - u(U_{Y'_j}) \le 0 \tag{24}$$

The mean and standard deviation of the t_c data for several bubbles were calculated directly from the experiments and by assuming a two-parameter (α, β) gamma cumulative distribution of the form:

$$F(t_c) = \frac{\gamma(t_c; \alpha, \beta)}{\Gamma(\alpha)} \tag{25}$$

where $\overline{t}_c = \alpha/\beta$ and $s(t_c) = \sqrt{\alpha/\beta^2}$. We calculated the experimental cumulative density function as:

$$\hat{F}(t_c) = \frac{1}{(N+1)} \sum_{\substack{i=0 \\ t_{c_i} < t_c}}^{N} 1 \tag{26}$$

and used it to determine α and β with their uncertainties at a 95% confidence level using the ODR method (Boggs et al., 1989).

3.4. Relevant dimensionless numbers

In this study, the relevant dimensionless numbers are Eötvös, Morton, Weber, and Reynolds, defined as:

$$Eo = \frac{\Delta\rho g \overline{d}_e^2}{\sigma} \tag{27}$$

$$Mo = \frac{g\nu_C^4(\rho_C - \rho_D)}{\rho_C^2 \sigma^3} = \frac{g\nu_C^4 \Delta\rho}{\rho_C^2 \sigma^3} \tag{28}$$

$$We = \frac{\rho_C \overline{U}_{Y'}^2 \overline{d}_e}{\sigma} \tag{29}$$

$$Re_d = \frac{\rho_C \overline{U}_{Y'} \overline{d}_e}{\nu_C} \tag{30}$$

3.5. Estimation of uncertainty of the image moments

Applying the generalized Reynolds transport theorem in the continuous formulation of the moments to calculate the variation of the moments m_{ij}, we have:

$$\delta\left(\iint_{\mathbb{D}} x^i y^j dx dy\right) = \iint_{\mathbb{D}} \delta(x^i y^j) dx dy + \iint_{\partial\mathbb{D}} x^i y^j (\delta \mathbf{r}_s \cdot \hat{\mathbf{n}}) dS \tag{31}$$

where $\partial\mathbb{D}$ is the boundary of $\mathbb{D}$, $\mathbf{r}_s$ is the position vector over $\partial\mathbb{D}$, $\hat{\mathbf{n}}$ is the outward unit vector normal to $\partial\mathbb{D}$, and S is the arc length along $\partial\mathbb{D}$. The last term in Eq. (31) is the contribution of the size variation of $\mathbb{D}$ in the moment variation.

The discrete form of Eq. (31) applied to a bubble with N_b pixels is:

$$\delta\left(\sum_{k=1}^{N_b} x_k^i y_k^j\right) = \sum_{k=1}^{N_b} \delta(x_k^i y_k^j) + \delta\left[\sum_{k=1}^{N_b} x_k^i y_k^j\right] \tag{32}$$

The uncertainty of m_{ij} comes from Eq. (32) as:

$$u\left(m_{ij}\right) = \sqrt{u^2\left(m_{ij}^{(\mathbb{D})}\right) + u^2\left(m_{ij}^{(\partial\mathbb{D})}\right)} \tag{33}$$

where

$$u^2\left(m_{ij}^{(\mathbb{D})}\right) = \sum_{k=1}^{N_b} u^2(x_k^i y_k^j), \tag{34}$$

and $u\left(m_{ij}^{(\partial\mathbb{D})}\right)$ is the uncertainty corresponding to the last term of Eq. (32). We approximated this term using the bubble's images with N_b^+ and N_b^- pixels, determined by the threshold perturbation analysis of the binarization process, shown in Section 3.2, giving:

$$u\left(m_{ij}^{(\partial\mathbb{D})}\right) = \frac{1}{2}\left[m_{ij}^{N_b^+} - m_{ij}^{N_b^-}\right] \tag{35}$$

where, in pixel units, we defined

$$m_{ij}^{N_b^\pm} = \sum_{k=1}^{N_b^\pm} x_k^i y_k^j \tag{36}$$

Using the uncertainties of the pixels' positions, $u(x_k)$ and $u(y_k)$, we can write:

$$u\left(x_k^i y_k^j\right) = x_k^i y_k^j \sqrt{\left(\frac{iu\left(x_k\right)}{x_k}\right)^2 + \left(\frac{ju\left(y_k\right)}{y_k}\right)^2} \tag{37}$$

which, by assuming that $u\left(x_k\right)$ and $u\left(y_k\right)$ are equal to the sensor's positioning uncertainty, $u(x)$, becomes:

$$\frac{u\left(x_k^i y_k^j\right)}{x_k^i y_k^j} = u(x)\left[\left(\frac{i}{x_k}\right)^2 + \left(\frac{j}{y_k}\right)^2\right]^{1/2} \tag{38}$$

Since $u(x)$ is quite small and the factor between brackets in Eq. (38) is also small for the lower order moments as $i << x_k$ and $j << y_k$, we neglected $u^2\left(m_{ij}^{(\mathbb{D})}\right)$ in Eq. (33), obtaining:

$$u\left(m_{ij}\right) = u\left(m_{ij}^{(\partial\mathbb{D})}\right) = \frac{1}{2}\left[m_{ij}^{N_b^+} - m_{ij}^{N_b^-}\right] \tag{39}$$

Similarly, we approximated the uncertainties of the central moments as:

$$u\left(\mu_{ij}\right) = u\left(\mu_{ij}^{(\partial\mathbb{D})}\right) = \frac{1}{2}\left[\mu_{ij}^{N_b^+} - \mu_{ij}^{N_b^-}\right] \tag{40}$$

where, in pixel units, we defined

$$\mu_{ij}^{N_b^\pm} = \sum_{k=1}^{N_b^\pm} (\Delta x_k)^i (\Delta y_k)^j \tag{41}$$

Appendix A gives details on the evaluation of the uncertainties of all bubble's characteristics, derived quantities, and dimensionless numbers described in Sections 3.3 and 3.4.

3.6. Numerical procedure

We implemented all image analysis and data processing in Python using some libraries: OpenCV (version 4.6.0.66) for thresholding and binarization, NumPy (version 1.23.1) and Pandas (version 1.4.3) for handling data arrays and data frames, SciPy (version 1.9.0) for performing regression using the ODR method (Boggs et al., 1989), and Matplotlib (version 3.5.2) for generating graphics.

We implemented the algorithm to process an image to obtain the binarized bubble image, determine its moments, calculate the perturbation to the binarization threshold, and determine the moments' uncertainties by recalculating the moments of binary bubble images obtained using perturbed thresholds. We validated the algorithm against images with known moments.

We also implemented the algorithm to determine the bubble's local vertical velocity using the bubble barycenter positions in a set of consecutive frames in a moving time window and the ODR package for model fitting.

Table 3
Configurations of the experimental data sets.

Configurations	Data Sets		
	I	II	III
Runs	1 – 30	31 – 35	36 – 40
f_{acq} (fps)	500	1000	1000
f_{pump} (steps/s)	50	10	10
Delay (s)	1.5	21.0	21.0
κ (px/mm)	23.0 ± 0.7	22.5 ± 0.6	49.9 ± 1.4
$\overline{T}$ (°C)	23.7 ± 0.3	23.0 ± 0.1	23.0 ± 0.1

4. Experimental data sets

We performed experiments using different camera acquisition frequencies, pump actuation speeds, and image resolutions. We organized the experimental runs into different data sets to determine the bubble characteristics, coalescence time, and number of bounces. For all experimental data sets, we employed a micro-Nikkor lens with a focal length of 60 mm, an effective aperture of $f/D = 16$, and an exposure time of 50 µs. The image resolution was 1280 × 800 pixels, $N_{frames} = 2500$ in single frame mode and $N_{steps} = 212$. For 212 steps in the syringe pump, the injected volume was 40.4 ± 1.5 µl, calculated by the pump volumetric calibration:

$$V_{inj} = N_{steps} R_v \tag{42}$$

where $R_v = 0.19 \pm 0.01$ µl/step is the pump volumetric resolution for the 1 ml syringe. The injected volume at each experimental run generated a unique bubble with an equivalent diameter of approximately 4.2 mm.

Table 3 lists other configurations used for the different data sets and gives the values for the scale factor. The reader should note that the scale factor error is approximately 3% for all experimental data sets. One of the configurations in Table 3 is the time delay between the activation of the syringe pump (first action) and the camera trigger (second action), which was necessary to capture the bubble's detachment, ascension, and coalescence with the interface. The mean operational temperature for all experiments was in the 23-25 °C range. Table 3 lists the $\overline{T}$ values for data sets I, II, and III.

Appendix B compares bubble volume via pump calibration and image processing for different pump actuation and acquisition frequencies. Results show that the mean bubble volume is independent of the injection flow rate up to 200 steps/s.

4.1. Configurations of the experimental data sets

For data set I, the total acquisition time was 5 s, and the injection time was 4.24 s. Therefore, the time delay of approximately 1.5 s allows for measuring coalescence times up to 2.26 s, which is the difference between the total acquisition time and the injection time plus the time delay.

To measure the bubble characteristics better, we reduced the pump actuation frequency by five times and increased the image acquisition frequency by twice in experimental data set II. For this data set, the total acquisition time was 2.5 s, and the injection time was 21.2 s. Therefore, a delay of approximately 21.0 s was necessary, allowing recording up to 2.3 s of the phenomenon.

We conducted experimental data set III to analyze the bubbles' bouncing at the interface with the highest possible resolution of our equipment by using the minimum focal length and rotating the camera

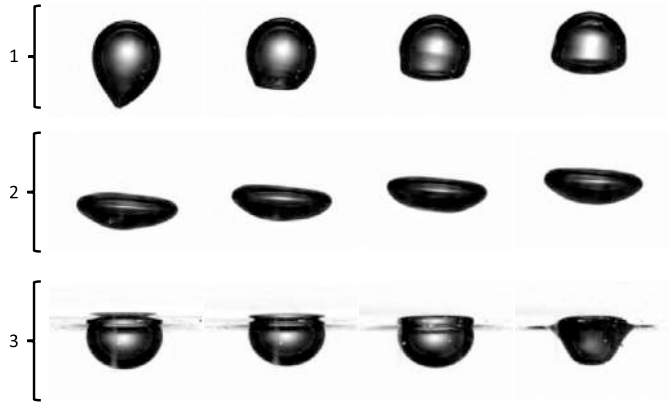

Fig. 7. Bubble behavior in coalescence experiments: 1 - Detachment, 2 - Ascension, 3 - Bouncing and coalescence.

90 degrees to maximize the number of pixels vertically. The scale factor obtained was almost double that of previous experiments. Additionally, we decreased the distance between the interface and the injection tube to obtain bubble approaching velocities lower than their terminal velocity.

5. Results and discussion

The Supplementary Material lists the results for the bubble characteristics, dimensionless numbers, and coalescence times of each run of experimental data sets I, II, and III.

5.1. Bubble behavior

Fig. 7 illustrates three stages of bubble behavior after detachment from the capillary until coalescence. The first stage occurs immediately after the detachment, where the lower part of the bubble moves much faster than the rest due to the action of the interfacial forces. In the second stage, the bubble deforms as it ascends through the fluid, assuming approximately the shape of a spheroid. The final stage involves the bubble's interaction with the interface, where its shape is approximately a spherical cap that oscillates and slides at the interface until coalescence. Furthermore, the interface deforms and is pushed upwards due to the bubble's presence.

Table 4
Static interface processing results.

Set	$Y_{int_{top}}$ [mm]	$Y_{int_{bottom}}$ [mm]	Y_{int} [mm]	Y_{tip} [mm]	H_{ris} [mm]
I	27.7 ± 0.1	26.5 ± 0.1	27.1 ± 0.6	2.11 ± 0.02	25.0 ± 0.6
II	28.4 ± 0.1	27.9 ± 0.1	28.1 ± 0.3	3.18 ± 0.02	24.9 ± 0.3
III	9.89 ± 0.01	8.37 ± 0.01	9.1 ± 0.8	1.17 ± 0.01	8.0 ± 0.8

5.2. Image processing validation

5.2.1. Static interface position

Table 4 presents the results of the image processing applied to images of the static air-water interface from experimental data sets I, II, and III, determined as described in Section 3.2.2. Table 4 lists the values for $Y_{int_{top}}$, $Y_{int_{bottom}}$, Y_{int}, Y_{tip} and H_{ris}, which are the vertical positions of the top, bottom and middle of the interface, the tip of the capillary tube, and the rising height. All vertical positions represent heights from the bottom of the image.

5.2.2. Bubble volume and velocity

We chose run 1 of the experimental data set I from Table 3 to exemplify the determination of the trajectories, volume, mean ascension velocity, and the vertical component of the instantaneous velocity of the rising bubbles.

Fig. 8a shows the bubble's trajectory through the X' and Y' coordinates of its centroid, while Fig. 8b depicts the vertical positions of the bubble's centroid, Y'_c, top surface, Y'_{top}, and bottom surface, Y'_{bottom}. As observed, the bubble follows an almost rectilinear trajectory until it approaches the interface. After the "collision", the bubble oscillates and slides at the interface, as shown by the displacement of Y'_{bottom} and the horizontal centroid position, X'_c, respectively.

Fig. 9 presents the results for the bubble's volume and ascension velocity of run 1. Figs. 9a and 9b represent $V \times Y'_c$ and $Y'_c \times t$ data, respectively, where V came from Eq. (15). The model given by Eq. (19) determined $\overline{U}_{Y'}$ from Fig. 9b data. The ODR method provides the standard deviation of $\overline{U}_{Y'}$ and its error at a 95% confidence level.

For all runs of data set I, Fig. 10a compares the mean bubble projected area estimated from the zeroth-order moment and the mean area determined from the ellipse's semi-axes determined from the image second-order central moments. For the same data, Fig. 10b compares the mean bubble volume obtained using the ellipse's area and the spheroidal shape hypothesis to the injected volume calculated from the pump calibration. Equation (18) calculates the mean values using all bubble images for a given run during its ascension. The volume injected by the pump was 40.4 ± 1.5 µl, obtained by the Eq. (42), and the light gray region in Fig. 10b represents its margin of error.

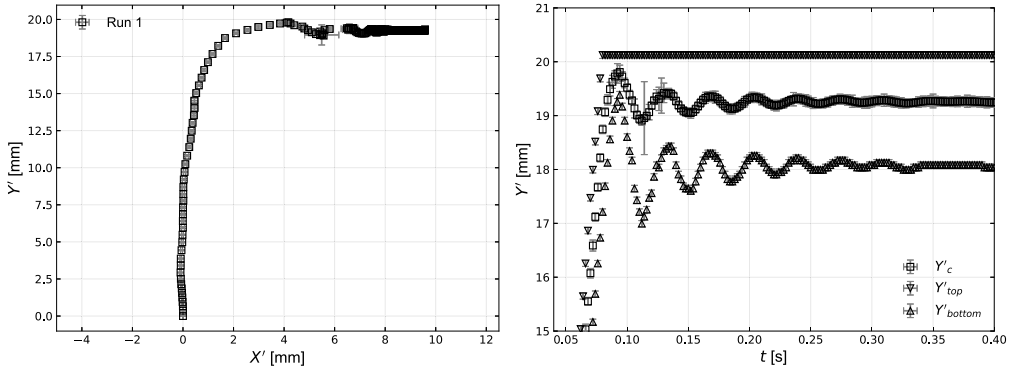

(a) X'_c and Y'_c (b) Y'_c, Y'_{bottom}, Y'_{top}

Fig. 8. Bubble's ascension: (a) trajectory of bubble barycenter, and (b) vertical positions of the bubble's centroid, top and bottom surfaces. Run 1 of experimental data set I.

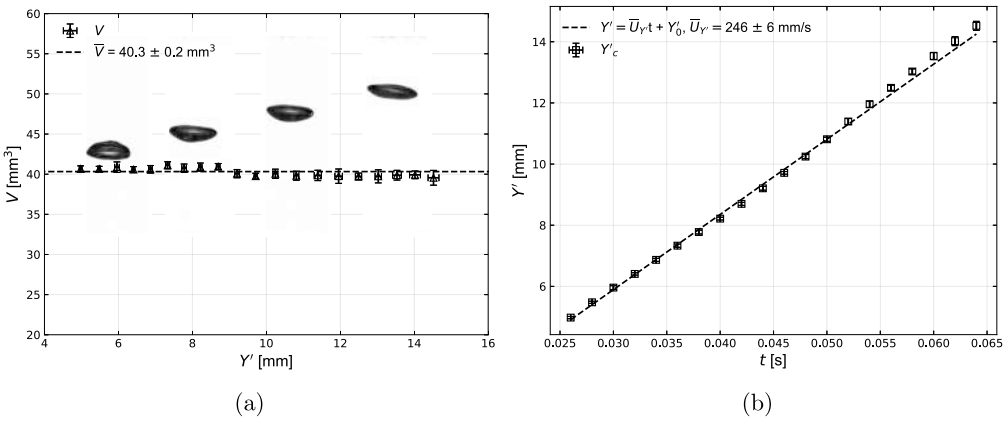

Fig. 9. Results for the bubble's (a) volume and (b) ascension velocity for run 1 in the experimental set I.

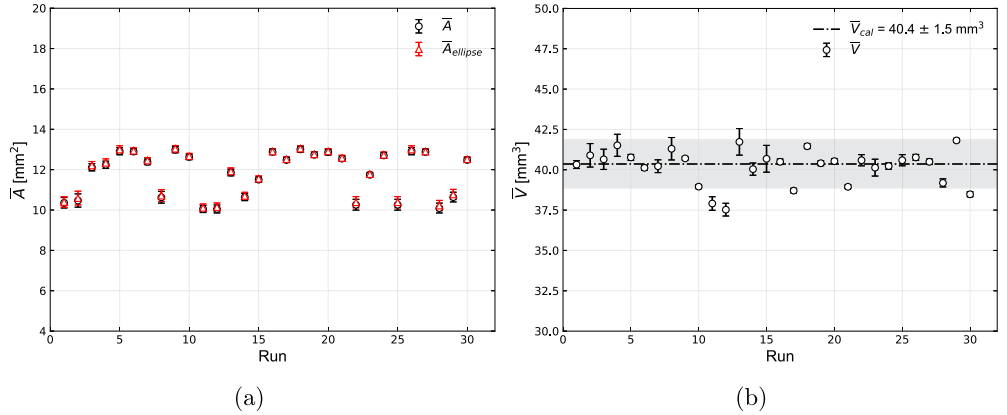

Fig. 10. Comparison of (a) bubbles' areas using image processing with and without the elliptical shape assumption and (b) their volumes using image processing and the injected volume determined from the syringe pump calibration for the experimental data set I.

For all runs of data set I, the mean bubble area obtained from the image zeroth-order moment and the elliptical approximation agree well. The bubble volume estimated from the injected volume for all runs of this data set also agrees well with the values estimated from image analysis, as most of them are equal within their margin of error. The difference between the mean volume of all runs and the injected volume is lower than 1%. The image processing determines a single bubble's volume more accurately than the predicted injected volume, as shown by the error bars in Fig. 10b. These results validate the hypothesis of elliptical and spheroidal shapes used to estimate the bubble's volumes from the images.

Fig. 11 compares the mean ascension velocity, $\overline{U}_{Y'}$, with the vertical component of the instantaneous velocity, $U_{Y'}$, calculated as described in Section 3.3.2 using the time intervals of $\Delta t_1 = 12$ and $\Delta t_2 = 16$ ms for runs 1 to 4 of experimental data set I. These intervals represent moving windows with seven and nine data points, respectively, as $\Delta t_{min} = 2$ ms for this experimental set. As can be seen, the velocity uncertainty decreases as Δt increases. The instantaneous velocity closely aligns with the mean velocity in the bubble's ascension period, decreasing when it approaches the interface. From 98.5 to 99.0% of the measured data points for each bubble satisfies the condition given by Eq. (20). Hence, we opted for the moving window with seven data points ($\Delta t = 12$ ms) to estimate the instantaneous bubbles' velocity. This interval yielded more local and less smooth results, even though with slightly larger errors than those using a moving window with nine data points. An increase in the frame acquisition rate might mitigate these errors. A less smoothed $U_{Y'}$ data is important for detecting its steep drop due to the bubble interaction with the interface.

Fig. 12 shows $U_{Y'}$ and the bubbles' top surface velocity, $U_{Y'_{top}}$, near the interface position, Y'_{int}, for runs 1 to 4 of the experimental set I. We used the time window with seven data points to calculate both vertical velocities. The shaded region corresponds to the Y'_{int} margin of error. As mentioned earlier, the error of $U_{Y'}$ increases as the distance between the bubble and the interface decreases due to the deviation of the data points from the employed linear model. Nevertheless, this approach gave the lowest error coefficients in the adjustment. Both $U_{Y'}$ and $U_{Y'_{top}}$ decrease, reaching zero when the bubble is at the interface.

In addition, Fig. 12 shows the "collision" instants detected by the PCC and the HCC. The PCC relies on the distance between the bubble top face and the static interface, while the HCC employs the velocity, considering their uncertainties. In all cases, the collision instant predicted by the PCC criterion precedes that of the HCC. Using the HCC, after reaching the interface, $U_{Y'}$ oscillates around zero until coalescence.

5.3. Effects of the injection flowrate and the image acquisition rate

To increase the accuracy of the bubble's characteristics, we obtained the experimental data set II using a pump actuation frequency five times lower (10 steps/s) and an image acquisition frequency twice higher (1000 fps) than those used in the experimental data set I.

Fig. 13 compares the equivalent diameter and mean ascension velocity determined from experimental data sets I and II with the results from Clift et al. (2005) for pure and contaminated water. In both experimental data sets, the experimental data for the bubbles' ascension velocity are within the range of ±10% of the bubble's terminal velocity for pure water. The accuracy and repeatability of the experimental data set I were 0.34% and 1.20%, respectively, while the corresponding

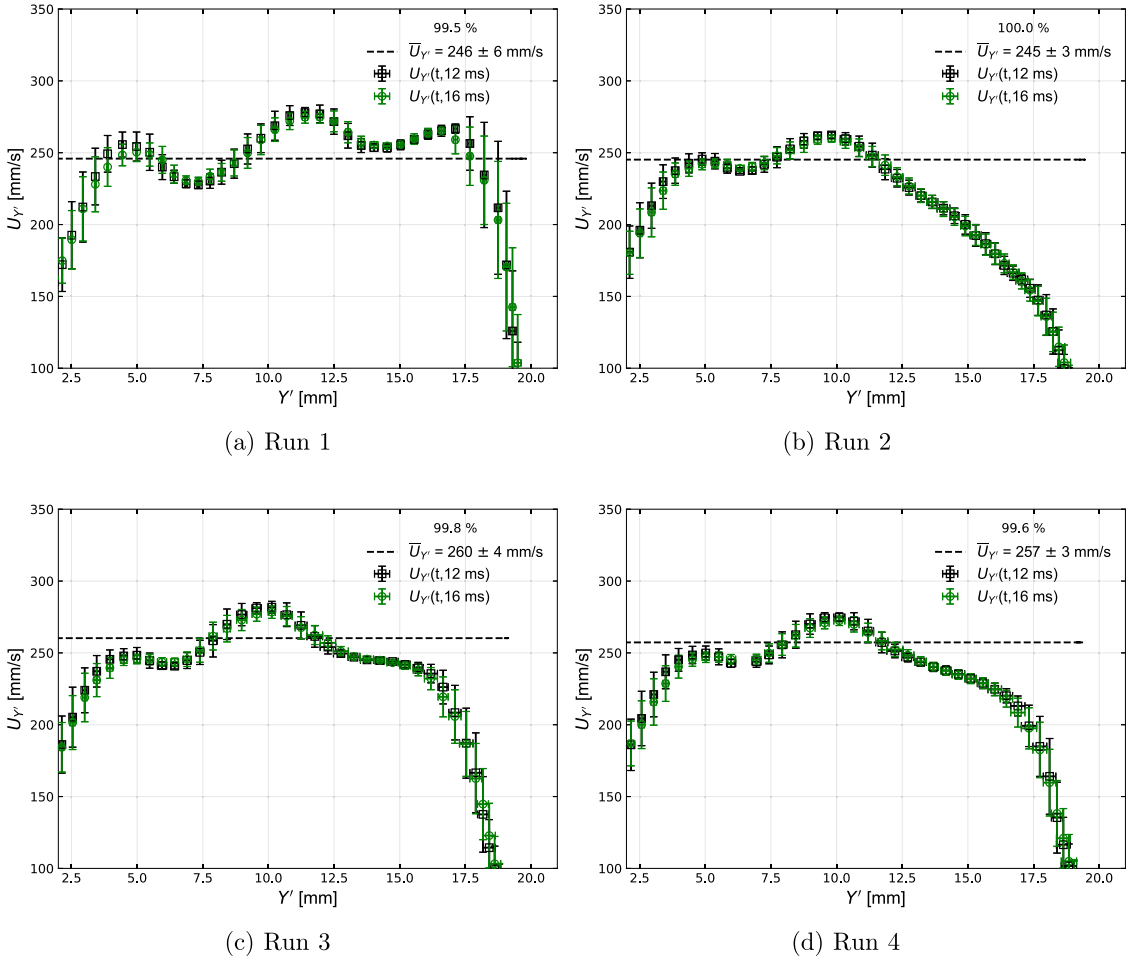

(a) Run 1 (b) Run 2

(c) Run 3 (d) Run 4

Fig. 11. Behavior of $U_{Y'} \times Y'$ against $\overline{U}_{Y'}$ calculated for the ascension stage. $U_{Y'}$ determined using $\Delta t = 12$ and 16 ms for four runs of the experimental set I, including the percentage of data agreement using these two intervals.

values for the experimental data set II were 0.83% and 0.23%. These results are in excellent agreement with previous knowledge, indicating that we managed to achieve the conditions of bubble ascension in pure water.

Fig. 14 shows the behavior of the bubbles' centroid, bottom, and top vertical positions over time near the interface for runs 1 and 2 of data set I and runs 31 and 32 for data set II. In experimental data set I, bubbles' bouncing is easily perceived, with amplitudes decreasing after each bounce. Although the terminal velocity and coalescence time results were better determined for the experimental data set II, observing the number of bubble bounces at the interface was difficult because of the small amplitude of bounces.

5.4. Coalescence time distribution at terminal velocity

Fig. 15 displays snapshots of the bubbles' at "collision" times as detected by both collision criteria, and at the coalescence time with the interface for runs 31, 32, and 33 of data set II. Figs. 15a and 15b show, respectively, the "collision" times according to PCC and HCC, and Fig. 15c shows the coalescence instants. The PCC detected the collision when the bubbles were farther from the interface. In contrast, the HCC detected it when the bubbles visually touched the interface, which is more consistent with forming a thin film between the bubble and the interface before coalescence.

Table 5 gives the estimated parameters for the gamma distribution using the coalescence times determined using both "collision" criteria. Both parameters were determined with uncertainties around 10-12%. Fig. 16 compares the adjusted cumulative distribution with the experimental cumulative density function using PCC and HCC. For both "collision" criteria, the empirical cumulative distributions and their adjusted gamma distribution exhibit similarity and agreement.

Table 5
Estimated parameters for the gamma distributions for $\bar{t}_c$ for data set I using both collision criteria.

Criterion	Parameters	
	$\alpha \pm u_{95}(\alpha)$	$\beta \pm u_{95}(\beta)$
PCC	3.9 ± 0.4	7.0 ± 0.8
HCC	3.7 ± 0.4	6.8 ± 0.9

Table 6 presents the mean value, $\bar{t}_c$, standard deviation, $s(t_c)$, and their uncertainties at the 95% confidence level for the coalescence time data calculated directly from the experiments and from the gamma distributions adjusted to the coalescence times determined using both "collision" criteria. The values of $\bar{t}_c$ and $s(t_c)$ obtained directly from the experimental data and from the gamma distribution agree well, but the $u_{95}(\bar{t}_c)$ values do not, being about 2.5 times smaller for the estimates using the gamma distributions.

5.5. Bubbles' bouncing analysis

We carried out the experiments of data set III (Runs 36, 37, 38, 39, and 40), with its larger image resolution, $\kappa = 49.9$ px/mm, to analyze bubbles' bouncing. Although the data set I experiments did not always allow us to count the number of bounces accurately, we managed to

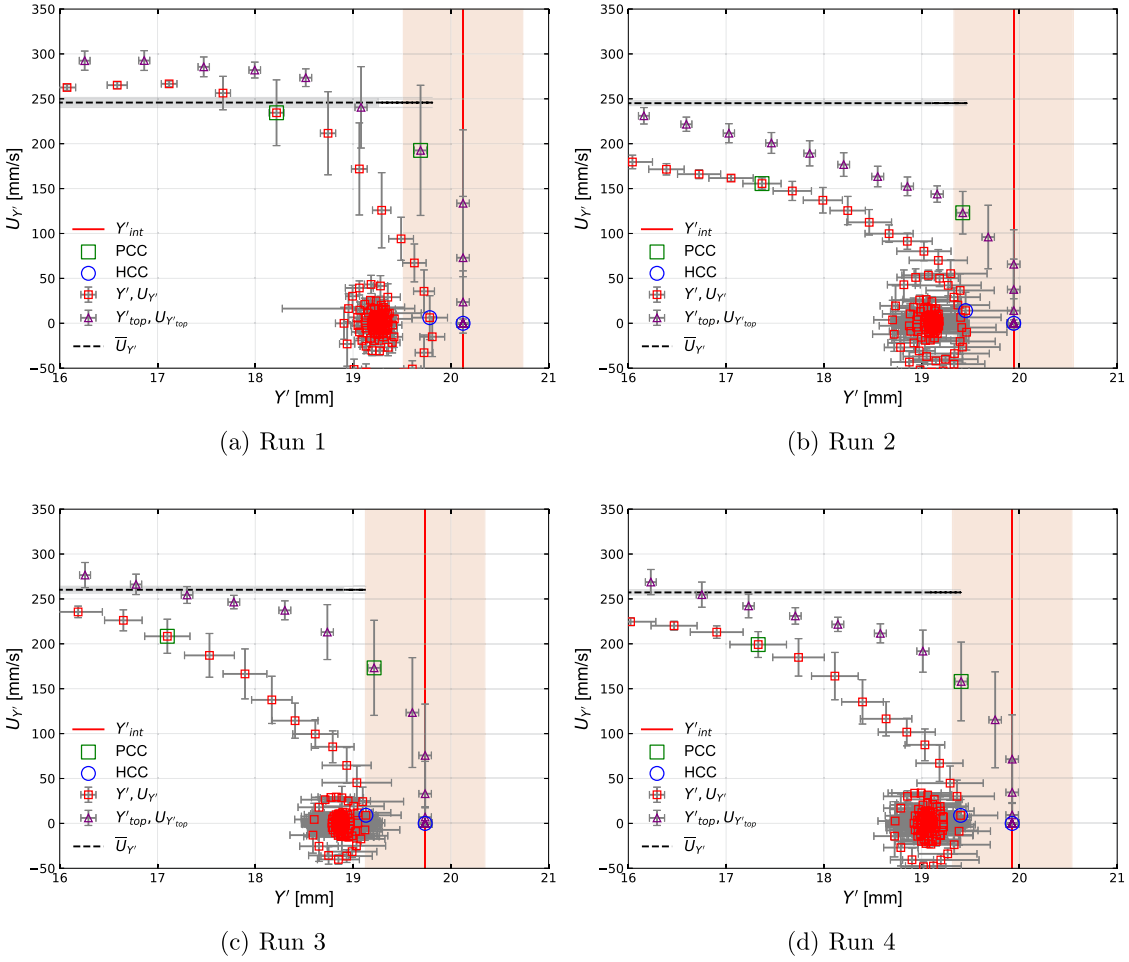

Fig. 12. Behaviors of $U_{Y'}$ and $U_{Y'_{top}}$ calculated using the seven-point moving window near the interface for four runs of experimental set I.

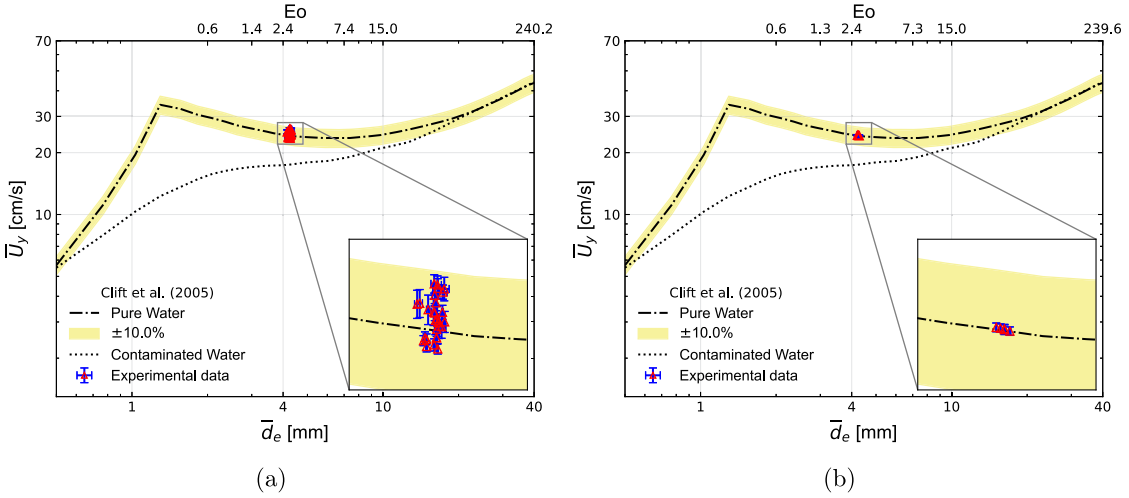

Fig. 13. Equivalent diameter and mean ascension velocity for the experimental data sets (a) I and (b) II.

Table 6
Coalescence time results for data set I using both collision criteria.

Criterion	Experimental results			Estimates from $F(t_c)$			
	$\overline{t}_c$	$s(t_c)$	$u_{95}(\overline{t}_c)$	$\overline{t}_c$	$u_{95}(\overline{t}_c)$	$s(t_c)$	$u_{95}(s)$
PCC	0.56	0.29	0.11	0.56	0.04	0.28	0.02
HCC	0.54	0.29	0.11	0.54	0.05	0.28	0.02

extract seven experiments (Runs 5, 8, 14, 16, 20, 23, and 24) for which we could count the number of bubble bounces. Besides, in data set III, the bubble rising height was smaller, making the bubbles' mean velocity at first "collision" with the interface about 60% of their terminal velocity (see Supplementary Material).

Table 7 presents the Morton and mean Weber numbers with their uncertainties at the 95% confidence level for data sets I and III. According

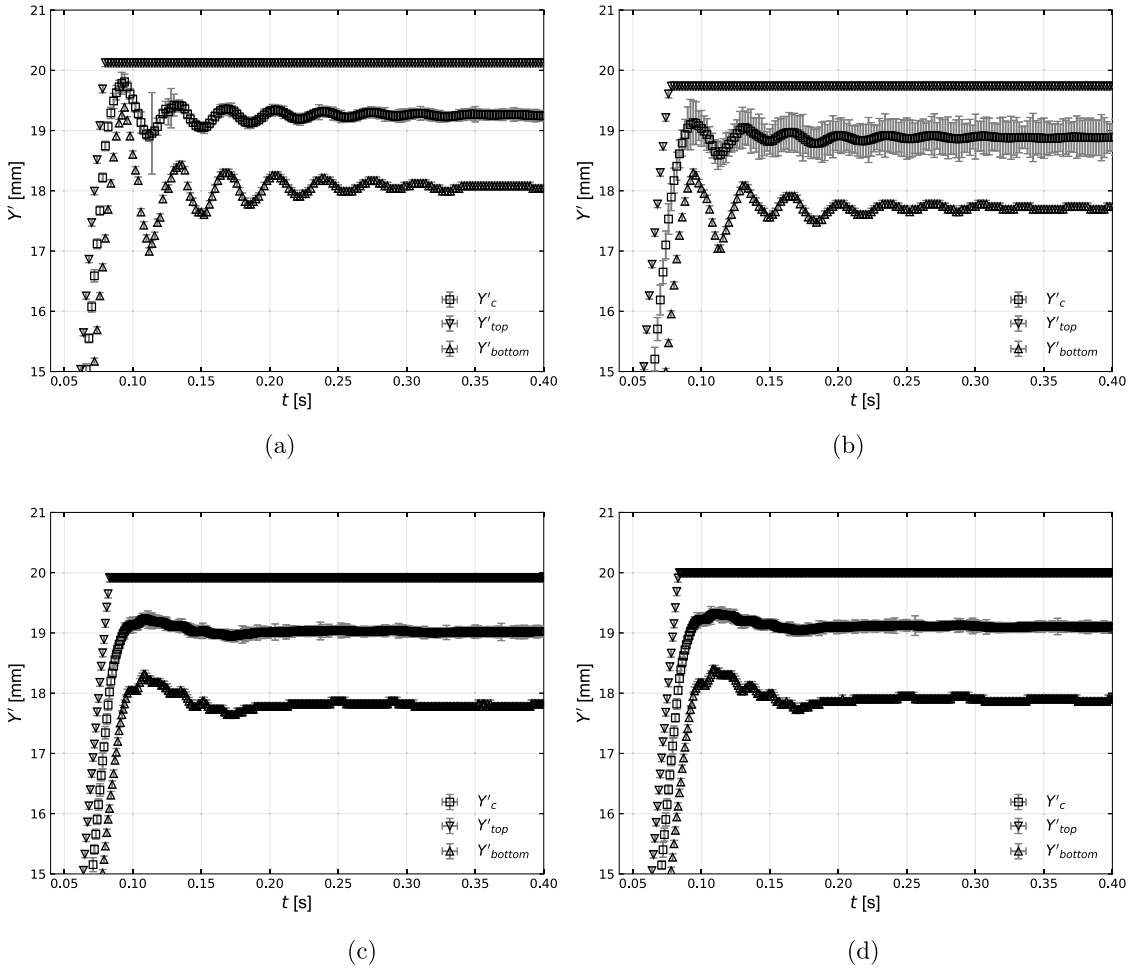

Fig. 14. Vertical positions of the bubbles' centroid (Y'_c), bottom surface (Y'_{bottom}), and top surface (Y'_{top}) for runs (a) 1 and (b) 2 of data set I, and runs (c) 31 and (d) 32 of data set II.

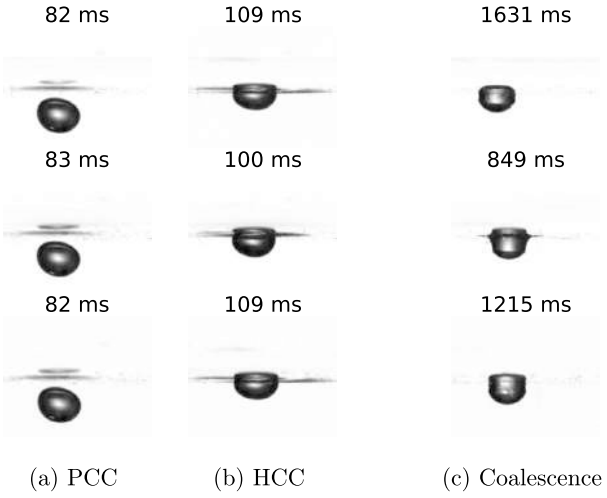

Fig. 15. Snapshots of bubbles from runs 31, 32, and 33 of data set II at "collision" times with the interface using the (a) PCC and (b) HCC, and (c) at coalescence times.

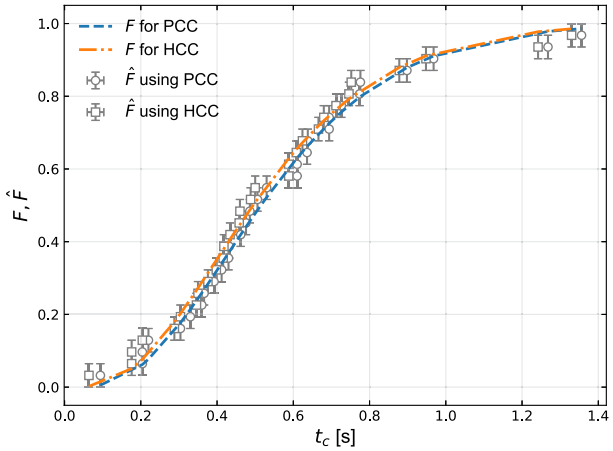

Fig. 16. Comparison between the "collision" time data obtained using PCC and HCC for data set I to the adjusted cumulative distributions.

to Horn et al. (2011), if the Weber number calculated with the bubble approaching velocity exceeds $We_{crit} \sim 1$, the bubble bounces. All our experiments were above this boundary, indicating bubble bouncing, which indeed occurred. The We values for the experiments in data set III were the nearest to the We_{crit} boundary, showing much lower coalescence times than those observed for the experimental data set I (see Supplementary Material).

Fig. 17 shows the vertical positions of the centroid, bottom surface, and top surface for the bubbles in runs 36 to 40 of data set III, organizing them according to the number of bounces. We counted the number of bounces at the interface before coalescence, considering the number of times the bubble approached the interface after the first collision. As

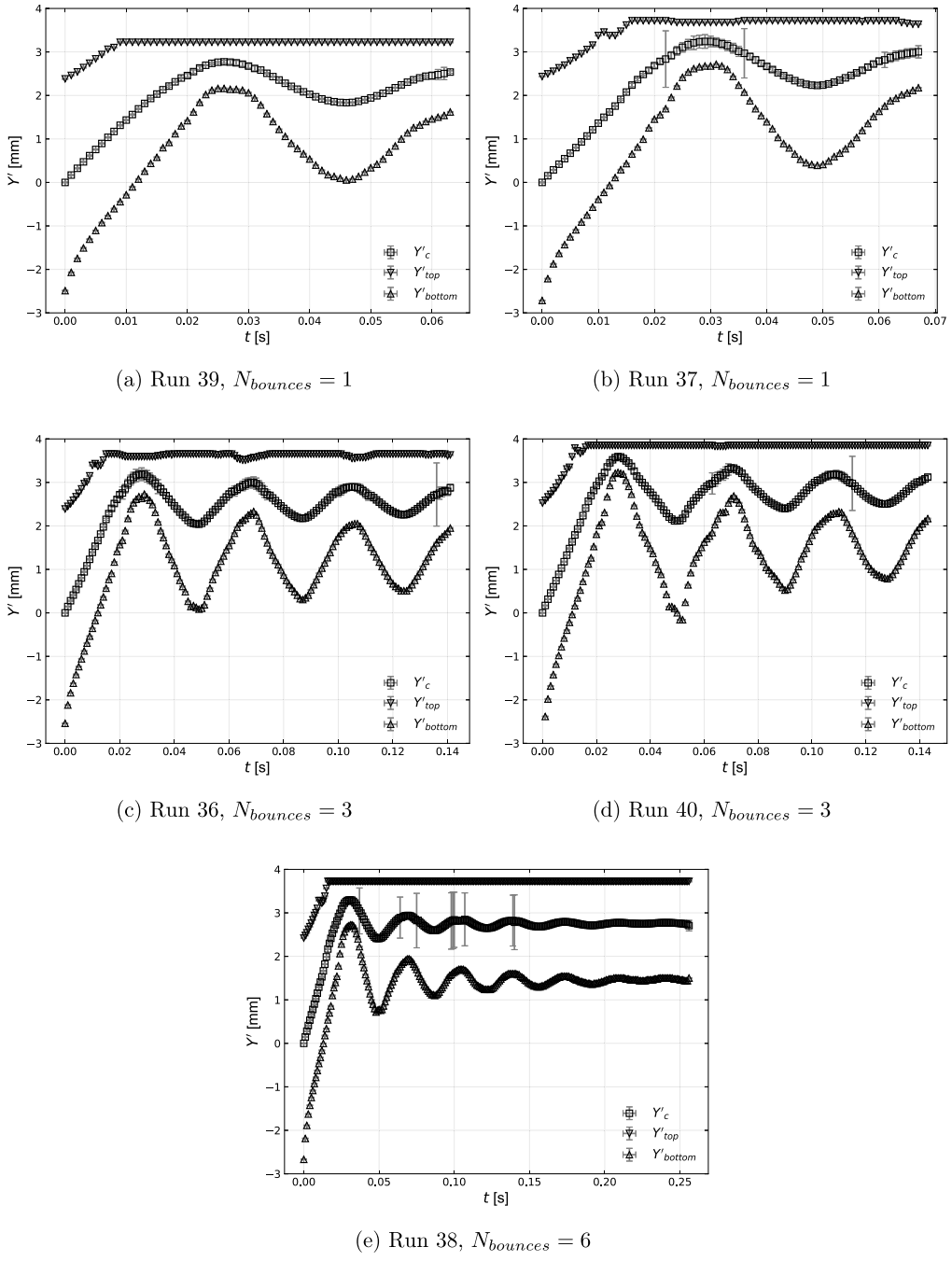

(a) Run 39, $N_{bounces} = 1$

(b) Run 37, $N_{bounces} = 1$

(c) Run 36, $N_{bounces} = 3$

(d) Run 40, $N_{bounces} = 3$

(e) Run 38, $N_{bounces} = 6$

Fig. 17. Behavior of the vertical position of the centroid (Y'_c), bottom face (Y'_{bottom}), and top face (Y'_{top}) of the bubbles until their coalescence with the interface for data set III.

Table 7
Morton and Weber numbers for experimental data sets I and III.

Set	$Mo \times 10^{11}$	$\overline{We}$
I	2.86 ± 0.03	3.62 ± 0.09
III	3.04 ± 0.03	1.26 ± 0.19

the amplitude decreases after each "collision", counting the bounces as their number increases becomes difficult. Even for the resolution of data set III, it was difficult to count a large number of bounces.

The reader can notice in Fig. 17 that the uncertainty in the vertical position of the bubble barycenter largely increases at some instants. Fig. 14 also shows the same behavior, although to a lesser extent. These larger uncertainties in Y'_c came from the increase in the uncertainties of the zeroth and first-order moments of the bubble image when its upper surface is close to the gas-liquid interface. We determined these larger uncertainties were due to lighting changes associated with bubble and interface deformations that affected the image binarization process. Nevertheless, the Y'_c values at such instants agree with those at neighbor points, which do not present such an increase in their uncertainties. Moreover, we could count the number of bubble bounces even for the runs that presented such behavior.

Sanada et al. (2009) stated that t_c increases with $N_{bounces}$. Thus, we assumed a linear relationship representing the $t_c(N_{bounces})$ dependency, testing linear models with two parameters and one parameter. For the latter, $t_c(0) = 0$, and it is given by:

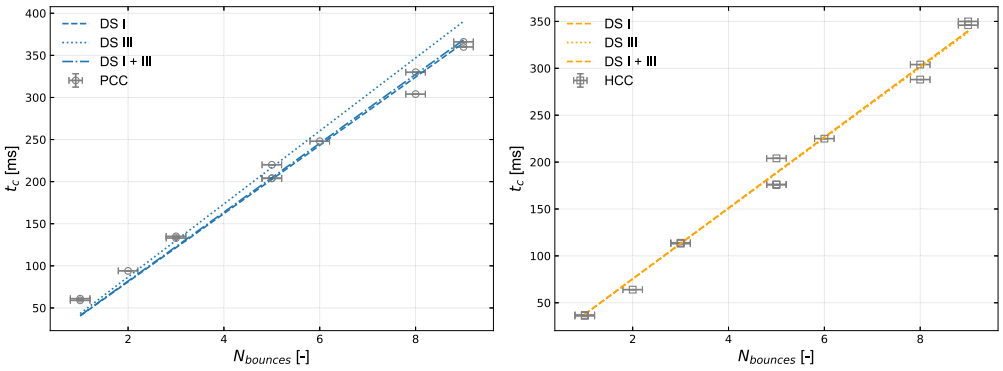

(a) Model PCC (b) Model HCC

Fig. 18. Fitted linear model between t_c and $N_{bounces}$ for the experimental data sets I, III, and I+III, using (a) PCC and (b) HCC.

Table 8
Comparison of resulting $\mathcal{T}$ from experiments.

	$\mathcal{T}$ [ms]		
	DS I	DS III	DS I+III
PCC	40.5 ± 1.4	43.4 ± 5.1	40.9 ± 1.4
HCC	37.8 ± 1.5	37.6 ± 0.4	37.7 ± 1.0

$$t_c = \mathcal{T} N_{bounces} \tag{43}$$

where $\mathcal{T}$ is the predicted bouncing period in milliseconds.

We fitted the two linear models to the available data for data sets I and III. In these data regressions, the standard uncertainty on the number of bounces was evaluated as type B, considering an error of unit and a triangular probability distribution. Only the Eq. (43) model correlated the available t_c data using HCC or PCC for both data sets with statistically significant parameter values, which occurs when the 95% confidence interval does not include zero. Therefore, we presented results only for this model.

Fig. 18 shows the fitted linear model for $t_c(N_{bounces})$ (Eq. (43)) using the experimental t_c data determined either using PCC or HCC for data sets I and III, either separately or together. Table 8 presents the parameter's values determined for these different data sets using both collision criteria.

Table 8 clearly shows that only the HCC led to a fitted model for both data sets with the same parameter value with low uncertainties. Besides, Fig. 18 shows that the fitted models for each data set or for the two data sets using HCC are identical, which does not occur for the t_c data obtained using PCC. Therefore, the linear model using the t_c data obtained using the HCC is more consistent with the available data.

We could not identify any relationship between the coalescence time of a bouncing bubble and its initial approaching velocity (see Tables 5 and 7 of the Supplementary Material).

5.6. Comparison with literature data

This section compares our data with those available in the literature, examining differences and similarities in bubble diameters, coalescence times, and the number of bounces.

The bubbles' diameter of 4 mm presented in this study is smaller than those in the experiments conducted by Kirkpatrick and Lockett (1974) for bubbles with a 5 mm diameter, but larger than those reported by Sanada et al. (2005), Suñol and González-Cinca (2010), Zawala and Malysa (2011) and Sato et al. (2011), who analyzed bubbles with diameters smaller than 2 mm.

Our experiments measured larger coalescence times than those reported in the literature, and our bubbles also bounced more on average.

In our experiments, the coalescence time ranged from 36 to 1550 ms for injection distances of 8.0 to 25.0 mm, with more than nine bounces observed. Kirkpatrick and Lockett (1974) reported coalescence times ranging from 150 to 180 ms for rising heights within 8.7 to 27.0 mm, where the bubble either coalesces on the first contact or oscillates twice before coalescence. On the other hand, Sanada et al. (2009) observed coalescence times from 0 to 60 ms with up to three bounces in low-viscosity liquids, and Zawala and Malysa (2011) reported coalescence times within 3 to 5 ms with up to five bounces. Suñol and González-Cinca (2010) measured coalescence times up to 100 ms with up to four bounces, and Sato et al. (2011) observed a maximum of four bubble bounces.

We could determine the bouncing period to be approximately 37.7 ms for bubbles with the same diameter but different approaching velocities. Only Kirkpatrick and Lockett (1974) reported the time interval between the first two "collisions" to be within 40 and 60 ms for similar rising heights. For Sanada et al. (2005) experiments with low-viscosity liquids, we estimated bouncing periods within 15 to 25 ms.

For small bubbles in the spherical regime, we expected that the coalescence time and the number of bounces would increase with the bubble size, as the bubble approaching velocity also tends to increase for the same rising height. For the ellipsoidal-wobbling bubble regime, this seems not to be true as Kirkpatrick and Lockett (1974) data and ours, both in this regime with the same range of rising heights, do not agree in the number of bounces or the coalescence time.

6. Conclusions

In this work, we analyzed the coalescence time of ellipsoidal-wobbling air bubbles with a surfactant-free flat air-water interface. The Morton number was 2.9×10^{-11}, and the ranges of Eötvös, Weber, and Reynolds dimensionless numbers were 2 to 3, 1 to 4, and 500 to 1100, respectively. We used high-speed fluid imaging techniques to measure the bubbles' size, velocity, and number of bounces at the interface. Two criteria to establish the time of the first collision with the interface were defined: the physical criterion, PCC, based on the distance between the top of the bubble and the static interface, and the hydrodynamic criterion, HCC, based on bubble velocity. We present results for the bubble volume, velocity, coalescence time, and number of bounces at the interface before coalescence.

The terminal velocity of the bubbles was close to its literature value for pure air-water systems under standard conditions. The distribution of coalescence time for the bubbles colliding at terminal velocity was estimated using both collision criteria. A two-parameter gamma distribution could represent the coalescence time data for both criteria.

We analyzed the relation between the coalescence time and the number of bubble bounces. We determined that a linear model with just one parameter, the bouncing period, can fit our data for both collision criteria. However, only the coalescence time obtained using the HCC gave the same low-uncertainty value for the bouncing period for two data

sets with quite different bubble-approaching velocities, making this criterion more consistent with our data. Using the two data sets and the HCC, the predicted bouncing period was 38 ± 1 milliseconds.

CRediT authorship contribution statement

Eric M.G. Fontalvo: Writing – review & editing, Writing – original draft, Visualization, Validation, Software, Methodology, Investigation, Formal analysis, Data curation, Conceptualization. **Paulo L.C. Lage:** Writing – review & editing, Writing – original draft, Software, Resources, Methodology, Formal analysis, Conceptualization. **Juliana B.R. Loureiro:** Writing – review & editing, Supervision, Resources, Formal analysis, Conceptualization.

Declaration of competing interest

The authors declare no known competing financial interests or personal relationships that could have appeared to influence the work reported in this paper.

Data availability

Some of the processed data is available in the Supplementary Material. Raw data can be made available upon request.

Acknowledgements

Eric M. G. Fontalvo thanks the Brazilian government agencies CNPq (process number 165784/2018-0) and CAPES (Finance Code 001), as well as the Colombian foundation COLFUTURO (PCB 2022), for the financial support granted during the development of this work. Paulo L. C Lage also thanks the financial support from CNPq, process number 303845/2022-8.

Appendix A. Evaluation of the bubble's characteristics and derived quantities uncertainties

We obtained the uncertainty of bubbles' derived quantities by propagation. For instance, for a generic variable equal to the product of other variables raised to a different power, such as $\varphi = \prod_{n=1}^{N} \chi_n^{\eta_n}$, we have:

$$\frac{u(\varphi)}{\varphi} = \sqrt{\sum_{n=1}^{N} \left(\frac{\eta_n u(\chi_n)}{\chi_n} \right)^2} \tag{A.1}$$

Hence, the propagation of the uncertainties of the image moments of order zero and one determined the standard combined uncertainty of the position coordinates of the bubble centroid (x_c', y_c') in pixel units. Similarly, the standard combined uncertainty of the vertical position of the bubble centroid in units of length resulted from the propagation of the uncertainty of the position in pixels and the uncertainty of the calculated scale factor. The scale factor uncertainty arises from combining the uncertainty of the calibration segment length with the uncertainty in the number of pixels in the segment, where their uncertainties stem from the resolution of the calibration target and the number of pixels for an error of unit, respectively, considering a triangular probability distribution.

The semiaxis uncertainties came from the propagation of the uncertainties of the eigenvalues of the central moments. In particular, the uncertainty of the eigenvalues $(\lambda_{1,2})$ are calculated as:

$$u\left(\lambda_{1,2}\right) = \sqrt{\left(\frac{\partial \lambda_1}{\partial \mu_{20}} u(\mu_{20}) \right)^2 + \left(\frac{\partial \lambda_1}{\partial \mu_{02}} u(\mu_{02}) \right)^2 + \left(\frac{\partial \lambda_1}{\partial \mu_{11}} u(\mu_{11}) \right)^2} \tag{A.2}$$

where

$$\frac{\partial \lambda_1}{\partial \mu_{20}} = \frac{1}{2} + \frac{\left(\mu_{20} - \mu_{02}\right)}{2\Delta\mu} \tag{A.3}$$

$$\frac{\partial \lambda_1}{\partial \mu_{02}} = \frac{1}{2} - \frac{\left(\mu_{20} - \mu_{02}\right)}{2\Delta\mu} \tag{A.4}$$

$$\frac{\partial \lambda_1}{\partial \mu_{11}} = \frac{2}{\Delta\mu} \mu_{11} \tag{A.5}$$

and

$$\Delta\mu = \sqrt{4\mu_{11}^2 + (\mu_{20} - \mu_{02})^2} \tag{A.6}$$

The uncertainty of the orientation of the ellipse's semi-axes came by propagating the uncertainties of the centered moments, being given as:

$$u(\theta) = \frac{1}{\Delta\mu^2} \sqrt{\mu_{11}^2 u^2(\mu_{20}) + \mu_{11}^2 u^2(\mu_{02}) + (\mu_{20} - \mu_{02})^2 u^2(\mu_{11})} \tag{A.7}$$

The propagation of the uncertainty of the ellipse's semi-axes lengths calculates the uncertainty of the ellipse's area. The bubble's volume uncertainty came from the uncertainty propagation of the semi-axes lengths of an oblate or prolate spheroid, depending on the orientation of its semi-axes. The uncertainty of the equivalent diameter was calculated from the volume uncertainty.

The uncertainty in the instantaneous vertical velocity came from the standard deviation of the parameter of the adjusted linear model obtained via ODR.

The uncertainty of the coalescence time came from propagating the uncertainty of the final time and the collision time. The uncertainty of any time instant is equal to the uncertainty of the camera's exposure time, assuming a triangular distribution. In addition, the uncertainty in any time interval, Δt, is $u(\Delta t) = \sqrt{2u^2(t)}$.

The relative uncertainty of the bubble-interface distance came from propagating the uncertainties of the interface and the top face bubble's position. The uncertainties of the dimensionless numbers are calculated by propagating the uncertainties of the bubbles' characteristics and the fluids' properties.

Finally, all the combined uncertainties were multiplied for a coverage factor to obtain the error range with 95% confidence level.

Appendix B. Comparison of bubbles' mean volumes from pump calibration and image processing

Two methods estimated the mean bubble volume: method 1, which employs the syringe pump calibration, and method 2, which uses the image processing described in Section 3.

B.1. Bubble volume from pump calibration (Method 1)

We calculated the mean bubbles' volume from pump calibration as the ratio of the injected volume divided by the number of bubbles generated during injection, $V_{cal} = V_{inj}/N_{bubbles}$, in which $N_{bubbles}$ can be obtained from image observation or signal treatment from image processing. The injected volume is the product of N_{steps} in each run and the pump volumetric resolution obtained previously through calibration, Eq. (42).

The uncertainty of the mean volume from pump calibration is obtained by propagating the uncertainties of the injected volume and the number of bubbles, where the uncertainties of N_{steps} and $N_{bubbles}$ were both evaluated as type B considering an error of unit and a triangular distribution.

B.2. Configuration of the experimental data set A

We performed two sets of five runs with camera acquisition frequencies of 50 and 500 fps and a pump injection speed of 50 steps/s. Table B.1 shows the configuration of these runs. The operational temperatures during the experiments were 22.58 ± 0.08 and 23.02 ± 0.08 °C for the runs with 50 and 500 fps acquisition frequencies, respectively.

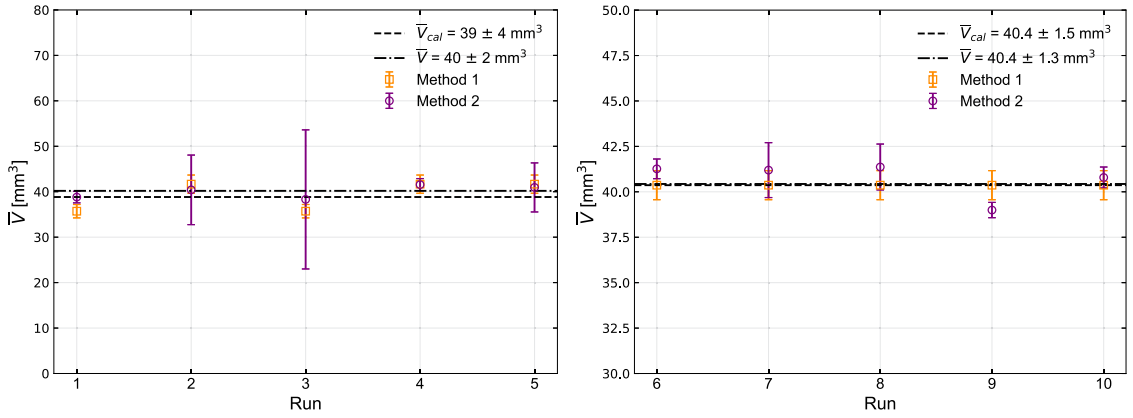

(a) 50 fps (b) 500 fps

Fig. B.1. Comparison of bubbles' volume obtained by the two methods for the experimental data set A.

Table B.1
Configuration of the experimental data set A. For all runs, $f_{pump} = 50$ steps/s, $\kappa = 23.0 \pm 0.7$ px/mm, and no time delay.

Run	f_{acq} (fps)	$N^{(*)}_{frames}$	N_{steps}
1 - 5	50	2000	1313
6 - 10	500	2500	212

(*) in single frame mode.

Table B.2
Average volume results for 50 fps and $V_{inj} = 250 \pm 9$ µl.

Run	$N_{bubbles}$	Method 1	Method 2	$\lvert\overline{V}_{cal} - V\rvert$ (µl)
		$\overline{V}_{cal}$ (µl)	$\overline{V}$ (µl)	
1	7	36 ± 2	39 ± 1	3
2	6	42 ± 2	40 ± 8	2
3	7	36 ± 2	38 ± 15	2
4	6	42 ± 2	42 ± 1	0
5	6	42 ± 2	41 ± 5	1

Table B.3
Average volume results for 500 fps and $V_{inj} = 40.4 \pm 1.5$ µl.

Run	$N_{bubbles}$	Method 1	Method 2	$\lvert\overline{V}_{cal} - V\rvert$ (µl)
		$\overline{V}_{cal}$ (µl)	$\overline{V}$ (µl)	
6	1		41.3 ± 0.5	0.9
7	1		41.2 ± 1.5	0.8
8	1	40.4 ± 1.5	41.4 ± 1.3	1.0
9	1		37.0 ± 0.4	3.4
10	1		40.8 ± 0.6	0.4

B.3. Bubble volume comparison

Tables B.2 and B.3 present the results of the mean volume of bubbles determined by methods 1 and 2 and their difference for the two sets of experiments of data set A. The volume injected for the runs with 50 and 500 fps was respectively 250 ± 9 and 40.4 ± 1.5 µl, calculated using Eq. (42).

In some experiments running at $f_{acq} = 50$ fps, 1 or 2 satellite bubbles formed during the injection of 6 or 7 bubbles, which increased the error in the mean volume obtained by the image analysis. For the runs at $f_{acq} = 500$ fps, only one bubble formed. In this case, the error in the bubbles' mean volume obtained by method 1 was larger than that obtained from the images by method 2.

Fig. B.1 compares the mean bubbles' volume calculated by both methods for the experiments at 50 and 500 fps of data set A. The mean bubbles' volumes obtained by methods 1 and 2 agree within their margins of error. The repeatability of the experiments was much better for the experiments at 500 fps, which generated only one bubble. The mean bubbles' volumes with both methods at both acquisition frequencies also agree within their error margins. These results strongly support the spheroidal bubble hypothesis.

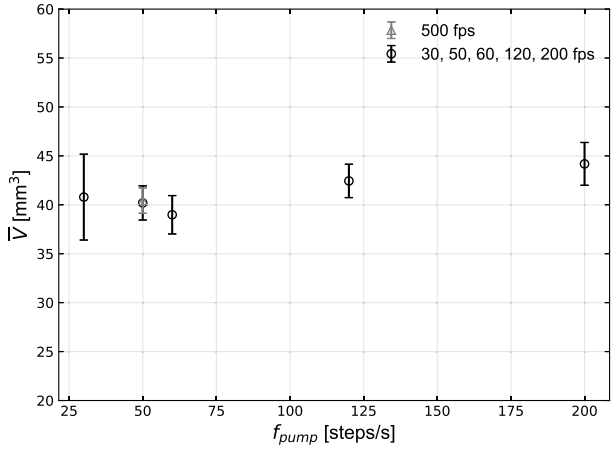

Fig. B.2. Bubble volume via image processing (method 2) as a function of the acquisition and pump frequency.

B.4. Bubbling regime

Fig. B.2 presents the mean bubbles' volume obtained via image processing (method 2) as a function of the syringe pump actuation frequency, which is proportional to the volumetric flowrate through the capillary tube. This figure includes the data from experiments using $f_{acq} = 50$ and 500 fps for $f_{pump} = 50$ steps/s and from other experiments, in which $f_{acq} = f_{pump}$ and equal to 30, 60, 120 and 200 fps or steps/s, respectively. These results show that the mean bubbles' volume is independent of the injection flow rate up to 200 steps/s, indicating that bubble formation occurred in the slow-bubbling regime, in which the interfacial force dominates the gas momentum influx.

Appendix C. Supplementary material

Supplementary material related to this article can be found online at https://doi.org/10.1016/j.ces.2024.120756.

References

Boggs, P.T., Donaldson, J.R., Byrd, R.h., Schnabel, R.B., 1989. Algorithm 676: Odrpack: software for weighted orthogonal distance regression. ACM Trans. Math. Softw. 15, 348–364. https://doi.org/10.1145/76909.76913.

Chesters, A., 1991. Modelling of coalescence processes in fluid-liquid dispersions: a review of current understanding. Chem. Eng. Res. Des. 69, 259–270.

Chesters, A., Hofman, G., 1982. Bubble coalescence in pure liquids. In: Mechanics and Physics of Bubbles in Liquids. Springer, The Netherlands, pp. 353–361.

Clift, R., Grace, J.R., Weber, M.E., 2005. Bubbles, Drops, and Particles. Courier Corporation.

Coelho, D.B., 2014. Projeto e construção de uma célula de coalescência de bolhas. Dissertação de mestrado. Universidade Federal do Rio de Janeiro.

Craig, V., Ninham, B., Pashley, R., 1993. Effect of electrolytes on bubble coalescence. Nature 364, 317–319. https://doi.org/10.1038/364317a0.

De Santo, M., Liguori, C., Paolillo, A., Pietrosanto, A., 2004. Standard uncertainty evaluation in image-based measurements. Measurement 36, 347–358. https://doi.org/10.1016/j.measurement.2004.09.011.

Doubliez, L., 1991. The drainage and rupture of a non-foaming liquid film formed upon bubble impact with a free surface. Int. J. Multiph. Flow 17, 783–803. https://doi.org/10.1016/0301-9322(91)90056-9.

Duineveld, P.C., 1994. Bouncing and coalescence of two bubbles in water. Ph.d. Thesis. Twente University, Netherlands.

Guinancio, R., 2015. Análise experimental de modelos de eficiência de coalescência de bolhas. Dissertação de mestrado. Universidade Federal do Rio de Janeiro.

Horn, R.G., Del Castillo, L.A., Ohnishi, S., 2011. Coalescence map for bubbles in surfactant-free aqueous electrolyte solutions. Adv. Colloid Interface Sci. 168, 85–92. https://doi.org/10.1016/j.cis.2011.05.006.

Hu, M.K., 1962. Visual pattern recognition by moment invariants. IRE Trans. Inf. Theory 8, 179–187. https://doi.org/10.1109/TIT.1962.1057692.

Joint Committee for Guides in Metrology, J., 2008. Guide to the Expression of Uncertainty in Measurement (GUM). Technical Report. Joint Committee for Guides in Metrology.

Jones, A., Wilson, S., 1978. The film drainage problem in droplet coalescence. J. Fluid Mech. 87, 263–288. https://doi.org/10.1017/S0022112078001585.

Kirkpatrick, R., Lockett, M., 1974. The influence of approach velocity on bubble coalescence. Chem. Eng. Sci. 29, 2363–2373. https://doi.org/10.1016/0009-2509(74)80013-8.

Lehr, F., Millies, M., Mewes, D., 2002. Bubble-size distributions and flow fields in bubble columns. AIChE J. 48, 2426–2443. https://doi.org/10.1002/aic.690481103.

Liao, Y., Lucas, D., 2010. A literature review on mechanisms and models for the coalescence process of fluid particles. Chem. Eng. Sci. 65, 2851–2864. https://doi.org/10.1016/j.ces.2010.02.020.

Liu, B., Manica, R., Liu, Q., Klaseboer, E., Xu, Z., 2019. Coalescence or bounce? How surfactant adsorption in milliseconds affects bubble collision. J. Phys. Chem. Lett. 10, 5662–5666. https://doi.org/10.1021/acs.jpclett.9b01598.

Liu, B., Manica, R., Xu, Z., Liu, Q., 2020. The boundary condition at the air-liquid interface and its effect on film drainage between colliding bubbles. Curr. Opin. Colloid Interface Sci. https://doi.org/10.1016/j.cocis.2020.07.003.

Malysa, K., Krasowska, M., Krzan, M., 2005. Influence of surface active substances on bubble motion and collision with various interfaces. Adv. Colloid Interface Sci. 114, 205–225. https://doi.org/10.1016/j.cis.2004.08.004.

Manica, R., Klaseboer, E., Chan, D.Y., 2016. The impact and bounce of air bubbles at a flat fluid interface. Soft Matter 12, 3271–3282. https://doi.org/10.1039/C5SM03151F.

Marrucci, G., 1969. A theory of coalescence. Chem. Eng. Sci. 24, 975–985. https://doi.org/10.1016/0009-2509(69)87006-5.

Mitre, J., Takahashi, R., Ribeiro Jr, C., Lage, P., 2010. Analysis of breakage and coalescence models for bubble columns. Chem. Eng. Sci. 65, 6089–6100. https://doi.org/10.1016/j.ces.2010.08.023.

Mitre, J.F., Lage, P.L., Souza, M.A., Silva, E., Barca, L.F., Moraes, A.O., Coutinho, R.C., Fonseca, E.F., 2014. Droplet breakage and coalescence models for the flow of water-in-oil emulsions through a valve-like element. Chem. Eng. Res. Des. 92, 2493–2508. https://doi.org/10.1016/j.cherd.2014.03.020.

Neethling, S., Cilliers, J., 2001. Simulation of the effect of froth washing on flotation performance. Chem. Eng. Sci. 56, 6303–6311. https://doi.org/10.1016/S0009-2509(01)00248-2.

Orvalho, S., Ruzicka, M.C., Olivieri, G., Marzocchella, A., 2015. Bubble coalescence: effect of bubble approach velocity and liquid viscosity. Chem. Eng. Sci. 134, 205–216. https://doi.org/10.1016/j.ces.2015.04.053.

Orvalho, S., Stanovsky, P., Ruzicka, M.C., 2021. Bubble coalescence in electrolytes: effect of bubble approach velocity. Chem. Eng. J. 406, 125926. https://doi.org/10.1016/j.cej.2020.125926.

Otsu, N., 1979. A threshold selection method from gray-level histograms. IEEE Trans. Syst. Man Cybern. 9, 62–66.

Reynolds, O., 1886. IV. On the theory of lubrication and its application to Mr. Beauchamp tower's experiments, including an experimental determination of the viscosity of olive oil. Philos. Trans. R. Soc. Lond. 177, 157–234. https://doi.org/10.1098/rstl.1886.0005.

Ribeiro Jr, C.P., Mewes, D., 2006. On the effect of liquid temperature upon bubble coalescence. Chem. Eng. Sci. 61, 5704–5716. https://doi.org/10.1016/j.ces.2006.04.043.

Ribeiro Jr, C.P., Mewes, D., 2007. The effect of electrolytes on the critical velocity for bubble coalescence. Chem. Eng. J. 126, 23–33. https://doi.org/10.1016/j.cej.2006.08.029.

Rubio, J., Souza, M., Smith, R., 2002. Overview of flotation as a wastewater treatment technique. Miner. Eng. 15, 139–155. https://doi.org/10.1016/S0892-6875(01)00216-3.

Sanada, T., Watanabe, M., Fukano, T., 2005. Effects of viscosity on coalescence of a bubble upon impact with a free surface. Chem. Eng. Sci. 60, 5372–5384. https://doi.org/10.1016/j.ces.2005.04.077.

Sanada, T., Sato, A., Shirota, M., Watanabe, M., 2009. Motion and coalescence of a pair of bubbles rising side by side. Chem. Eng. Sci. 64, 2659–2671. https://doi.org/10.1016/j.ces.2009.02.042.

Sato, A., Shirota, M., Sanada, T., Watanabe, M., 2011. Modeling of bouncing of a single clean bubble on a free surface. Phys. Fluids 23. https://doi.org/10.1063/1.3546019.

Suñol, F., González-Cinca, R., 2010. Rise, bouncing and coalescence of bubbles impacting at a free surface. Colloids Surf. A, Physicochem. Eng. Asp. 365, 36–42. https://doi.org/10.1016/j.colsurfa.2010.01.032.

Suñol, F., González-Cinca, R., 2019. Effects of gravity level on bubble detachment, rise, and bouncing with a free surface. Int. J. Multiph. Flow 113, 191–198. https://doi.org/10.1016/j.ijmultiphaseflow.2019.01.016.

Tripathi, M.K., Sahu, K.C., Govindarajan, R., 2015. Dynamics of an initially spherical bubble rising in quiescent liquid. Nat. Commun. 6, 1–9. https://doi.org/10.1038/ncomms7268.

Vakarelski, I.U., Manica, R., Li, E.Q., Basheva, E.S., Chan, D.Y., Thoroddsen, S.T., 2018. Coalescence dynamics of mobile and immobile fluid interfaces. Langmuir 34, 2096–2108. https://doi.org/10.1021/acs.langmuir.7b04106.

Vakarelski, I.U., Yang, F., Thoroddsen, S.T., 2020. Free-rising bubbles bounce stronger from mobile than immobile water-air interfaces. Langmuir. https://doi.org/10.1021/acs.langmuir.0c00668.

Versluis, M., 2013. High-speed imaging in fluids. Exp. Fluids 54, 1–35. https://doi.org/10.1007/s00348-013-1458-x.

Wang, H., Yang, W., Yan, X., Wang, L., Wang, Y., Zhang, H., 2020. Regulation of bubble size in flotation: a review. J. Environ. Chem. Eng., 104070. https://doi.org/10.1016/j.jece.2020.104070.

Yang, W., Luo, Z., Lai, Q., Zou, Z., 2019. Study on bubble coalescence and bouncing behaviors upon off-center collision in quiescent water. Exp. Therm. Fluid Sci. 104, 199–208. https://doi.org/10.1016/j.expthermflusci.2019.02.016.

Zawala, J., Malysa, K., 2011. Influence of the impact velocity and size of the film formed on bubble coalescence time at water surface. Langmuir 27, 2250–2257. https://doi.org/10.1021/la104324u.

Zhang, X.B., Luo, Z.H., 2020. Effects of bubble coalescence and breakup models on the simulation of bubble columns. Chem. Eng. Sci. 115850doi. https://doi.org/10.1016/j.ces.2020.115850.